ELSEVIER

Space–time discontinuous Galerkin discretization of rotating shallow water equations

V.R. Ambati *, O. Bokhove

Numerical Analysis and Computational Mechanics Group, Department of Applied Mathematics, University of Twente, P.O. Box 217, Enschede, The Netherlands

Abstract

A space–time discontinuous Galerkin (DG) discretization is presented for the (rotating) shallow water equations over varying topography. We formulate the space–time DG finite element discretization in an efficient and conservative discretization. The HLLC flux is used as numerical flux through the finite element boundaries. When discontinuities are present, we locally apply dissipation around these discontinuities with the help of Krivodonova's discontinuity indicator such that spurious oscillations are suppressed. The non-linear algebraic system resulting from the discretization is solved using a pseudo-time integration with a second-order five-stage Runge–Kutta method. A thorough verification of the space–time DG finite element method is undertaken by comparing numerical and exact solutions. We also carry out a discrete Fourier analysis of the one-dimensional linear rotating shallow water equations to show that the method is unconditionally stable with minimal dispersion and dissipation error. The numerical scheme is validated in a novel way by considering various simulations of bore–vortex interactions in combination with a qualitative analysis of PV generation by non-uniform bores. Finally, the space–time DG method is particularly suited for problems where dynamic grid motion is required. To demonstrate this we simulate waves generated by a wave maker and verify these for low amplitude waves where linear theory is approximately valid.
© 2007 Elsevier Inc. All rights reserved.

1. Introduction

For waves and currents in oceans, coastal zones and rivers with small depth and vertical velocity scales relative to typical horizontal scales, the hydrodynamics can be studied using (rotating) shallow water equations [15]. These equations are a two dimensional hyperbolic system modeling the depth and depth-averaged

---

* Corresponding author. Tel.: +31 534893397; fax: +31 534894833.
  E-mail addresses: v.r.ambati@math.utwente.nl (V.R. Ambati), o.bokhove@math.utwente.nl (O. Bokhove).

horizontal velocities for an incompressible fluid. Due to this hyperbolic nature, discontinuities can develop in the form of bores or hydraulic jumps. They exist as weak solutions [22] and are considered, in near-shore hydrodynamics, as mathematical analogs of the three dimensional wave breaking observed at beaches. The shallow water wave model is one of the simplest models to capture natural wave phenomena such as run-up and backwash of the shoreline at beaches, coastal waves and tides and floods induced by hurricanes and tsunamis. These phenomena usually take place in a complex shaped domain with a combination of fixed and freely moving boundaries, where the moving boundaries are due to the movement of the shoreline. To cope accurately with these complexities, we present a space–time discontinuous Galerkin method for simulating shallow water waves on a dynamic spatial grid. The free boundary treatment is left to the future study but as a preliminary step we consider moving boundaries due to a wave maker (see also [5]).

The space–time discontinuous Galerkin method [24] can accurately model inviscid compressible fluid flows in a time dependent flow domain. In this method, we tessellate the space–time domain with space–time finite elements and on such an element we define the local basis functions to approximate the flow field and test functions. As a result, the space–time weak formulation results into element volume and face integrals per space–time element. Communication between elements arises via a numerical flux. There are several choices of numerical fluxes; here we have chosen the HLLC flux because it is accurate and efficient compared with other approximate Riemann solvers (see [4,24,21]). This HLLC flux results in an upwind flux in the time direction ensuring the causality of time.

The finite element discretization of the weak formulation results in a set of coupled non-linear algebraic equations per space–time element. These equations are then solved locally by adding a pseudo-time derivative and integrating in pseudo-time until a steady state is reached. We use the five-stage second-order accurate Runge–Kutta time integration scheme defined in [24]. The convergence acceleration of the pseudo-time integration scheme towards steady state can be quite slow without special attention, yet at a reasonable computation time compared to explicit space DG schemes. However, we have left the implementation of a multi-grid algorithm [24,14] to accelerate the convergence of the pseudo-time integration as future work.

Numerically, spurious oscillations are expected to appear only around hydraulic jumps or bores. To limit these spurious oscillations, a dissipation operator of Jaffre et al. [8] is added to the discretization, as in Van der Vegt and Van der Ven [24] where it operates everywhere but very mildly in smooth regions and strongly around discontinuities. In contrast, we apply the dissipation operator where the discontinuity detector of Krivodonova et al. [9] informs us to apply it. This more strongly preserves the higher order accuracy in smooth regions and suppresses the spurious oscillations around discontinuities. The crucial difference between space and space–time discontinuous Galerkin finite element methods is that in the latter case time is also treated with a finite element instead of a finite difference method. Further, space and time are treated in unison with space–time basis functions, here polynomials in space and time. Preservation of non-negative or positive depths has received a lot of attention in finite-volume modelling (e.g. [3]). It has the disadvantage that even when land must fall dry, it will always stay covered with "numerical" water. This may lead to a robust scheme but effectively leads to mass loss. Bokhove [5] therefore only ensures positive mean depths in an element, but does allow the slope of the depth to indicate where dry regions may appear in a space discontinuous Galerkin method. Problematic (e.g., in [5]) is the finite difference discretization in time, which only allows a wet region with positive depth to become a region with negative depth after one (intermediate) time step. The space–time method has the advantage of a finite element method in which the water line is known in space and time.[1]

Novel is that the space–time discontinuous Galerkin method is presented for rotating shallow water waves over varying bottom topography in fixed and time dependent flow domains. To preserve the hydrostatic balance of the rest state over arbitrary topography, and uniform flow of water over a flat bottom, at the discrete level, we approximate the topography smoothly with a linear polynomial basis based on a nodal approximation per element. Discrete Fourier analysis of the present numerical method for linear rotating shallow water equations in one dimension is carried out to show that the method is unconditionally stable and has minimal dispersion error and dissipation.

---

[1] By combining local mesh adaptation and a non-negative approach in pseudo-time, we aim to deal much more accurately with flooding and drying. Initial tests are encouraging [1].

Furthermore, the accuracy of the numerical scheme is thoroughly verified in a comparison with some known exact and approximate solutions. We simulate the harmonic modes of linearized (rotating) shallow water equations, which includes Kelvin and Poincaré modes under low amplitude for a number of time periods to show qualitatively that the scheme has minimal dispersion error and dissipation. Rotating shallow water flows dissipate energy in the presence of bores or jumps and generate PV anomaly in the case of non-uniform bores (see [16,17]). Such bore–vortex interactions are considered as necessary, advanced and demanding test cases in which non-uniform bores are formed and subsequently PV is generated (see [7]).

This paper is organized as follows: the shallow water equations, their conservation laws and the generation of PV by non-uniform bores are discussed in Section 2. The space–time discontinuous Galerkin finite element method in a time dependent computational domain is presented in Section 3. A discrete Fourier analysis and the persistence of the steady rest state over smooth topography are shown in Section 4. The numerical scheme is verified in Section 5. The PV anomaly generated by non-uniform bores is validated in Section 6. Conclusions follow in Section 7.

2. Rotating shallow water flows

2.1. Mathematical model

The rotating shallow water equations in the conservative form are (see [15])

$$\mathbf{V} \cdot \mathscr{F}_i(\mathbf{U}) = S_i \quad \text{in } \Omega \subset \mathbb{R}^2, \tag{1}$$

where $\mathbf{V} = (\partial_t, \partial_x, \partial_y)^{\mathrm{T}}$ is the differential operator, $\mathbf{U} = (h, hu, hv)^{\mathrm{T}}$ the state vector, $h(\mathbf{x})$ the water depth, $\mathbf{u}(\mathbf{x}) = (u(\mathbf{x}), v(\mathbf{x}))^{\mathrm{T}}$ the velocity field,

$$\mathscr{F}(\mathbf{U}) = \begin{pmatrix} \mathscr{F}_0(\mathbf{U}) \\ \mathscr{F}_1(\mathbf{U}) \\ \mathscr{F}_2(\mathbf{U}) \end{pmatrix} = \begin{pmatrix} h & hu & hv \\ hu & hu^2 + gh^2/2 & huv \\ hv & huv & hv^2 + gh^2/2 \end{pmatrix} \text{ the flux tensor,}$$

$$S = (S_0, S_1, S_2)^{\mathrm{T}} = (0, \mathrm{f}hv - gh\partial_x h_\mathrm{b}, -\mathrm{f}hu - gh\partial_y h_\mathrm{b})^{\mathrm{T}}$$

the source vector, g the gravitational acceleration, f the Coriolis parameter, $h_\mathrm{b}(\bar{\mathbf{x}})$ the bottom topography and $\mathbf{x} = (t, \bar{\mathbf{x}}) = (t, x, y)$ the space–time coordinates. Finally, we complete the system (1) with inflow, outflow or solid wall boundary conditions at the boundary $\partial\Omega \subset \mathbb{R}$ and initial conditions $\mathbf{U}(0, \bar{\mathbf{x}})$.

For numerical calculations, we non-dimensionalize the equations with typical length L, time T, depth H and velocity V scales as

$$t' = t/T, \quad \bar{\mathbf{x}}' = \bar{\mathbf{x}}/L, \quad h' = h/H, \quad h_\mathrm{b}' = h_\mathrm{b}/H, \quad \mathrm{f}' = \mathrm{f}T \quad \text{and} \quad \mathbf{u}' = \mathbf{u}/V, \tag{2}$$

where $V = \sqrt{gH}$ and $T = L/\sqrt{gH}$. Substituting (2) in (1) and dropping the primes, the non-dimensionalized shallow water equations effectively become (1) with $g = 1$ and $\mathrm{f} \to \mathrm{f}T$.

2.2. Conservation laws

The shallow water equations (1) govern the conservation of mass and momentum of the system. In the absence of discontinuities, the shallow water equations conserve energy, absolute vorticity and enstrophy

$$\partial_t \begin{pmatrix} \widetilde{E} \\ h\Pi \\ hQ \end{pmatrix} + \overline{\nabla} \cdot \begin{pmatrix} (\widetilde{E} + gh^2/2)\mathbf{u} \\ h\mathbf{u}\Pi \\ h\mathbf{u}Q \end{pmatrix} \quad \text{in } \Omega \subset \mathbb{R}^2, \tag{3}$$

where the energy

$$\widetilde{E}(\mathbf{x}) := h|\mathbf{u}|^2/2 + gh^2/2 + ghh_\mathrm{b}, \tag{4}$$

potential vorticity $\Pi(\mathbf{x}) := (\Omega_v + \mathrm{f})/h$, absolute vorticity $\Omega_v(\mathbf{x}) = \partial_x v - \partial_y u$, potential enstrophy $Q(\mathbf{x}) := \Pi^2/2$ and $\overline{\nabla} := (\partial_x, \partial_y)^{\mathrm{T}}$. Furthermore, potential vorticity is materially conserved, i.e.,

$$\partial_t \Pi + \mathbf{u} \cdot \overline{\nabla} \Pi = 0 \quad \text{in } \Omega. \tag{5}$$

2.3. Bore–vortex anomaly

We concisely write (1) as $\partial_t \mathbf{U} + \overline{\nabla} \cdot \mathbf{F}(\mathbf{U}) = S$ with $\mathbf{U}$ the temporal and $\mathbf{F}(\mathbf{U})$ the spatial part of the flux vector $\mathscr{F}$. The shallow water equations (1) admit discontinuities in the form of tidal bores in coastal seas or hydraulic jumps in river channels, or may develop discontinuities in finite time from smooth initial data as bores formed due to wave breaking phenomena. These discontinuities are weak solutions of the conservation law $\partial_t \mathbf{U} + \overline{\nabla} \cdot \mathbf{F}(\mathbf{U}) = 0$. For smooth topography, they satisfy the Rankine–Hugonoit relations [12] given by

$$[\![\bar{\mathbf{n}} \cdot \mathbf{F}(\mathbf{U}) - V_n \mathbf{U}]\!] = [\![S]\!] = 0, \tag{6}$$

where $\bar{\mathbf{n}}$ is the unit space normal vector at point $\bar{\mathbf{x}}_c$ on the discontinuity curve pointing from 1 to 2, as in Fig. 1, $V_n = \mathbf{V} \cdot \bar{\mathbf{n}}$ the normal velocity of the discontinuity, $\mathbf{V} = (V_x, V_y)^T$ the velocity of the discontinuity and $[\![\cdot]\!]$ the jump defined as $[\![q]\!] := q_1 - q_2$ with $q_1 = \lim_{\epsilon \downarrow 0} q(t, \bar{\mathbf{x}}_c - \epsilon\bar{\mathbf{n}})$ and $q_2 = \lim_{\epsilon \downarrow 0} q(t, \bar{\mathbf{x}}_c + \epsilon\bar{\mathbf{n}})$ the traces of q taken from either side of the discontinuity. Applying (6) for the mass and momentum conservation laws (1), we obtain the following jump relations across the bore [19,25]:

$$[\![h(\mathbf{u} \cdot \bar{\mathbf{n}} - V_n)]\!] = 0 \quad \text{and} \quad \left[\!\left[h(\mathbf{u} \cdot \bar{\mathbf{n}})(\mathbf{u} \cdot \bar{\mathbf{n}} - V_n) + \frac{1}{2}gh^2 \right]\!\right] = 0. \tag{7}$$

Introducing the normal velocity of water particles relative to the moving bore as $\hat{u} = \mathbf{u} \cdot \bar{\mathbf{n}} - V_n$ and solving the relations (7), we obtain

$$Q^2 := (h_1 \hat{u}_1)^2 = (h_2 \hat{u}_2)^2 = g h_1 h_2 (h_1 + h_2)/2 \tag{8}$$

with h_1 and h_2 the depths adjacent to the bore, and discharge Q across.

In the presence of discontinuities, the jump relations of the energy, vorticity and enstrophy conservation laws are not satisfied and hence they are not conserved. Instead, for the energy conservation law in (3), if we evaluate the L.H.S. of the Rankine–Hugonoit relation (6) then we obtain the rate of energy dissipation across the bore as (see also [11,20])

$$QE_D = [\![(\widetilde{E} + gh^2/2)(\mathbf{u} \cdot \bar{\mathbf{n}}) - V_n \widetilde{E}]\!] = gQ(h_2 - h_1)^3/(4h_1 h_2) \tag{9}$$

with E_D the energy dissipation per unit discharge across the bore. To obtain the physically meaningful solution, we have to assume that the energy dissipation $QE_D > 0$ for $h_1 \neq h_2$, since the energy flux $[\![(\widetilde{E} + gh^2/2)(\mathbf{u} \cdot \bar{\mathbf{n}})]\!]$ through the bore should always be greater than $[\![V_n \widetilde{E}]\!]$ the rate of change of energy at the bore. Further, for uniqueness, we have to assume that the water particles crossing the bore should always lose energy [20]. Hence, for $Q > 0$ we have $h_1 < h_2$ and for $Q < 0$ we have $h_1 > h_2$, since we must have $QE_D > 0$. This is the energy dissipating condition analogous to the entropy condition in gas dynamics.

Peregrine [16] shows that the jump in PV $[\![\Pi]\!] = \Pi_1 - \Pi_2$ can be calculated by modification of Kelvin's circulation theorem to obtain

$$[\![\Pi]\!] = \Delta\Pi = -\frac{1}{Q}\frac{dE_D}{d\hat{y}} \tag{10}$$

with local coordinates $\hat{\mathbf{x}} = (\hat{x}, \hat{y})^T$ and $\hat{y}$ aligned along the tangent of the bore.
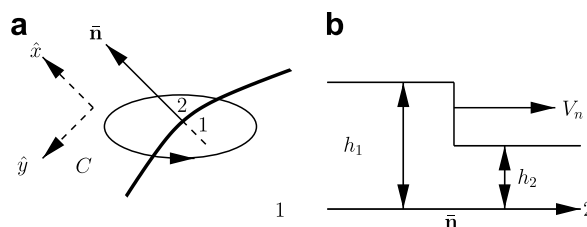

Fig. 1. A sketch of a bore along with stream lines (a), a contour C, and traces of the upstream and downstream flow field at the bore (b).

Hence, if there was no PV in the water undisturbed by the bore then Π_2 is the new nonzero PV when $Q > 0$ and, vice versa, Π_1 is the new nonzero PV when $Q < 0$. Bühler [6] shows that only PV anomalies can be generated by bores, such that the total PV remains the same in the absence of sources or sinks of PV other than the bores and hydraulic jumps. In the numerical simulations, we qualitatively verify the generation of PV due to non-uniform energy dissipation along the bore.

3. Space–time DG finite element model

3.1. Space–time tessellation, function spaces, traces and trace operators

The space–time flow domain $\mathscr{E}$ is defined as $\mathscr{E} := \{(t, \bar{\mathbf{x}}) | \bar{\mathbf{x}} \in \Omega(t), t_0 < t < T\} \subset \mathbb{R}^3$ with $\Omega(t) \subset \mathbb{R}^2$ the flow domain, t_0 the initial time and T the final time. To tessellate the space–time domain, the time interval $[t_0, T]$ is divided into N_T finite time intervals $I_n = [t_n, t_{n+1}]$ with $n = 0, \ldots, N_T$. Now at each time level t_n, we tessellate the flow domain $\Omega(t_n)$ using the open space elements K_k^n with closure $\bar{K}_k^n$ to obtain a mesh with N_e spatial elements. The space–time tessellation consisting of space–time elements $\mathscr{K}_k^n$ can be obtained by connecting the corresponding spatial elements K_k^n and K_k^{n-1} of the computational space domain Ω_h at times t_n and t_{n-1}. It is convenient to map each space–time element $\mathscr{K}_k^n$ onto a reference element $\hat{\mathscr{K}}$ with its coordinates $(\zeta_0, \zeta_1, \zeta_2)$ in which ζ_0 corresponds to time t. We choose quadrilaterals as the spatial elements and thus we obtain hexahedrals as the space–time elements.

To define the discontinuous Galerkin weak formulation, we introduce the broken space $\mathscr{V}_h^d$ defined as $\mathscr{V}_h^d := \{\mathbf{V}_h | \mathbf{V}_h |_{\mathscr{K}} \in (P^1(\mathscr{K}))^d\}$ with P^1 the space of linear polynomials, $d = \dim(\mathbf{V}_h)$ and $\mathbf{V}_h$ the polynomial approximation per space–time element defined as $\mathbf{V}_h := \sum_{m=0}^{M-1} \widehat{\mathbf{V}}_m \psi_m(\mathbf{x})$, where $\widehat{\mathbf{V}}_m$ is the expansion coefficient, $\psi_m(\mathbf{x})$ the polynomial basis functions and M the number of basis functions. The basis functions are chosen such that the local finite element space on $\mathscr{K}_k^n$ is either of span $\{1, t, x, y, xy\}$ with $M = 5$ for fixed meshes or of span $\{1, t, x, y, xy, tx, ty, txy\}$ with $M = 8$ for dynamic meshes (see [24] for definitions). Such a span allows us to approximate functions as piecewise continuous and linear on a space–time hexahedral mesh, which is particularly useful to approximate the bottom topography $h_b(\bar{\mathbf{x}})$.

To calculate the flux through the element boundaries, it is useful to introduce the union of faces $\mathscr{S}_m$, each face either connecting two space–time elements, known as interior face, or a space–time element to the boundary of the space–time domain $\partial\mathscr{E}$, known as boundary face. The union of all faces $\mathscr{S}_m$ is $\Gamma = \Gamma_{\text{int}} \cup \Gamma_{\text{bou}}$ with Γ_{int} and Γ_{bou} the union of interior and boundary faces, respectively. It is also useful to define the trace of the function $\mathbf{V}_h$ on the element boundary $\partial\mathscr{K}_k^n$ taken from the inside of the space–time element $\mathscr{K}_k^n$ as

$$\mathbf{V}_h(\mathbf{x})|_{\partial\mathscr{K}_k^n} = \mathbf{V}^- := \lim_{\epsilon \uparrow 0} \mathbf{V}_h(\mathbf{x} + \epsilon \mathbf{n}_{\mathscr{K}}) \tag{11}$$

with $\mathbf{n}_{\mathscr{K}}$ the outward unit normal vector of the boundary $\partial\mathscr{K}_k^n$. Since $\mathbf{V}_h \in \mathscr{V}_h^d$, i.e., the functions are approximated per space–time element $\mathscr{K}_k^n$, the traces of the function taken from the inside of any two adjacent elements are discontinuous. Hence, on each face $\mathscr{S}_m$ connecting the element $\mathscr{K}^l$ from left and $\mathscr{K}^r$ from right, it is convenient to introduce the following weighted average $\{\!\{\cdot\}\!\}$ and jump $[\![\cdot]\!]$ trace operators:

Definition 1. The weighted average $\{\!\{F\}\!\}_{\alpha,\beta}$ of a scalar function $F \in \mathscr{V}_h^d$ and $\{\!\{\mathbf{G}\}\!\}_{\alpha,\beta}$ of a vector function $\mathbf{G} \in \mathscr{V}_h^d$ on $\mathscr{S}_m \in \Gamma_{\text{int}}$ are defined as

$$\{\!\{F\}\!\}_{\alpha,\beta} := (\alpha F^l + \beta F^r) \quad \text{and} \quad \{\!\{\mathbf{G}\}\!\}_{\alpha,\beta} := \alpha \mathbf{G}^l + \beta \mathbf{G}^r \tag{12}$$

with $\alpha + \beta = 1$; and F^l and F^r the traces of the scalar function F, and $\mathbf{G}^l$ and $\mathbf{G}^r$ the traces of the vector function $\mathbf{G}$ taken from the inside of elements $\mathscr{K}^l$ and $\mathscr{K}^r$, respectively.

Definition 2. The jump $[\![F]\!]$ of a scalar function $F \in \mathscr{V}_h^d$ and $[\![\mathbf{G}]\!]$ of a vector function $\mathbf{G} \in \mathscr{V}_h^d$ on $\mathscr{S}_m \in \Gamma_{\text{int}}$ are defined as

$$[\![F]\!] := (F^l \mathbf{n}_{\mathscr{K}}^l + F^r \mathbf{n}_{\mathscr{K}}^r) \quad \text{and} \quad [\![\mathbf{G}]\!] := \mathbf{G}^l \cdot \mathbf{n}_{\mathscr{K}}^l + \mathbf{G}^r \cdot \mathbf{n}_{\mathscr{K}}^r \tag{13}$$

with $\mathbf{n}_{\mathscr{K}}^{l}$ and $\mathbf{n}_{\mathscr{K}}^{r}$ the outward unit normal vectors of the face $\mathscr{S}_m$ w.r.t. elements $\mathscr{K}^l$ and $\mathscr{K}^r$, respectively. Note that $\mathbf{n}_{\mathscr{K}}^{l} = -\mathbf{n}_{\mathscr{K}}^{r}$. Now the following relation holds between jumps and averages:

$$F^{l}(\mathbf{G}^{l} \cdot \mathbf{n}_{\mathscr{K}}) + F^{r}(\mathbf{G}^{r} \cdot \mathbf{n}_{\mathscr{K}}^{r}) = \{\!\{F\}\!\}_{\alpha,\beta}[\![\mathbf{G}]\!] + [\![F]\!] \cdot \{\!\{\mathbf{G}\}\!\}_{\beta,\alpha}, \quad \mathscr{S}_m \in \Gamma_{\text{int}}. \tag{14}$$

3.2. Discontinuous Galerkin weak formulation

The discontinuous Galerkin weak formulation per space–time element $\mathscr{K}_k^n$ is obtained by multiplying the shallow water equations (1) with arbitrary test functions $\mathbf{W}_h \in \mathscr{V}_h^d$, integrating by parts over space–time element $\mathscr{K}_k^n$, using Gauss' theorem in space and time, introducing the shorthand notation $\mathscr{F}_i(\mathbf{U}^-) = \mathscr{F}_i^-$, and summing up over all space–time elements. We obtain then the weak formulation as

Find a $\mathbf{U}_h \in \mathscr{V}_h^d$ such that for all

$$\sum_{\mathscr{S}} \left\{ \iint_{\mathscr{S}_m} \widehat{F}_i(\mathbf{U}^l, \mathbf{U}^r, \mathbf{n}_{\mathscr{K}})(W_i^l - W_i^r) \, \mathrm{d}\mathscr{S} \right\} - \sum_{\mathscr{K}} \left\{ \int_{\mathscr{K}_k^n} \nabla W_{hi} \cdot \mathscr{F}_i(\mathbf{U}_h) \, \mathrm{d}\mathscr{K} + \int_{\mathscr{K}_k^n} W_{hi} S_i \, \mathrm{d}\mathscr{K} \right\} = 0$$

$$\forall \mathbf{W}_h \in \mathscr{V}_h^d \tag{15}$$

is satisfied.

In obtaining the weak formulation (15), we have rearranged the element boundary integrals into a summation of interior and boundary face integrals, used the relation (14), enforced the continuity of the flux $[\![\mathscr{F}_i]\!] = 0$ and introduced a consistent and conservative numerical flux as

$$\widehat{F}_i(\mathbf{U}^l, \mathbf{U}^r, \mathbf{n}_{\mathscr{K}}) \approx \mathbf{n}_{\mathscr{K}} \cdot \{\!\{\mathscr{F}_i\}\!\}_{\alpha,\beta} \quad \text{for } \mathscr{S}_m \in \Gamma_{\text{int}} \text{ and } \mathbf{n}_{\mathscr{K}} \cdot \mathscr{F}_i^l \text{ for } \mathscr{S}_m \in \Gamma_{\text{bou}}, \tag{16}$$

where $\mathscr{F}^K$, $\mathbf{U}^K$ and W^K are the limiting trace values on the face $\mathscr{S}_m$ taken from the inside of the element $\mathscr{K}^K$, $K = l$ or r; and, $\mathbf{n}_{\mathscr{K}}$ is the unit normal vector. In Section 3.4, we will define the normal numerical flux $\widehat{F}_i(\mathbf{U}^l, \mathbf{U}^r, \mathbf{n}_{\mathscr{K}})$ through the faces. The weak formulation (15) is akin to the numerical implementation in which we loop separately over faces and elements to calculate the face and element integrals.

3.3. Numerical dissipation near bores and jumps

In numerical discretizations of the weak formulation (15), spurious oscillations generally appear near discontinuities. To suppress these spurious oscillations, we extend and apply the dissipation operator of Van der Vegt and Van der Ven [24] into the weak formulation per space–time element $\mathscr{K}_k^n$ as

$$\mathscr{D}_k^n(\mathbf{W}_h, \mathbf{U}_h; \mathbf{U}_h^*) := \int_{\mathscr{K}_k^n} (\nabla U_{hi})^{\mathrm{T}} \mathfrak{D}_k^n(\mathbf{U}_h, \mathbf{U}_h^*)(\nabla W_{hi}) \, \mathrm{d}\mathscr{K}, \tag{17}$$

where $\mathfrak{D}_k^n(\mathbf{U}_h, \mathbf{U}_h^*)$ is the diagonal dissipation matrix, $\mathbf{U}_h$ the solution in $\mathscr{K}_k^n$ and $\mathbf{U}_h^*$ the solution in the immediate neighboring elements of $\mathscr{K}_k^n$. The dissipation operator (17) acts in every space–time element $\mathscr{K}_k^n$ but is only required around discontinuities and sharp gradients.

The evaluation of the numerical dissipation operator $\mathscr{D}_k^n(\mathbf{W}_h, \mathbf{U}_h, \mathbf{U}_h^*)$ is more straightforward in the reference coordinate directions than in the physical space coordinates, so we transform (17) onto the reference element as

$$\mathscr{D}_k^n(\mathbf{W}_h, \mathbf{U}_h; \mathbf{U}_h^*) := \int_{\widehat{\mathscr{K}}} (\widehat{\nabla} U_{hi})^{\mathrm{T}} (J^{-1} \mathfrak{D}_k^n(\mathbf{U}_h, \mathbf{U}_h^*)(J^{\mathrm{T}})^{-1})(\widehat{\nabla} W_{hi}) |J| \, \mathrm{d}\widehat{\mathscr{K}} \tag{18}$$

with J the Jacobian matrix defined as $J_{kl} := \partial x_k / \partial \zeta_l$, $|J|$ the determinant of the Jacobian matrix, $\widehat{\nabla} = (\partial_{\zeta_0}, \partial_{\zeta_1}, \partial_{\zeta_2})^{\mathrm{T}} = J^{\mathrm{T}} \nabla$. Now, we introduce the dissipation matrix $\widetilde{\mathfrak{D}}_k^n(\mathbf{U}_h, \mathbf{U}_h^*)$ on the reference element as $\widetilde{\mathfrak{D}}_k^n(\mathbf{U}_h, \mathbf{U}_h^*) := J^{-1} \mathfrak{D}_k^n(\mathbf{U}_h, \mathbf{U}_h^*)(J^{\mathrm{T}})^{-1}$. To evaluate (18) with less computational effort, we compute $\widetilde{\mathfrak{D}}_k^n(\mathbf{U}_h, \mathbf{U}_h^*)$ only at the midpoint of the reference element $\zeta = (0, 0, 0)$ at which the Jacobian matrix is diagonalized as $J = \mathrm{diag}\{c_0, c_1, c_2\}/2$ with $c_k = 2\sum_{l=0}^3 \partial x_k / \partial \zeta_l$. Since $\mathfrak{D}_k^n(\mathbf{U}_h, \mathbf{U}_h^*)$ is a diagonal matrix, the dissipation matrix $\widetilde{\mathfrak{D}}_k^n(\mathbf{U}_h, \mathbf{U}_h^*)$ is simplified to

$$\widetilde{\mathfrak{D}}_{k;kl}^{n}(\mathbf{U}_{h}, \mathbf{U}_{h}^{*})|_{\zeta=(0,0,0)} := \frac{4}{\mathsf{c}_{k}^{2}} \mathfrak{D}_{k,kk}^{n}(\mathbf{U}_{h}, \mathbf{U}_{h}^{*}) \quad \text{for } k = l, \text{ and } 0 \text{ for } k \neq l. \tag{19}$$

Jaffre et al. [8] proposed a diagonal dissipation matrix $\mathfrak{D}_{k}^{n}(\mathbf{U}_{h}, \mathbf{U}_{h}^{*})$ for hyperbolic conservation laws, which is defined as

$$\mathfrak{D}_{k;kk}^{n}|_{(\zeta=0,0,0)} := \begin{cases} \max(C_{2}\mathsf{c}_{\mathscr{K}}^{2-\gamma} \mathscr{R}_{k}^{n}(\mathbf{U}_{h}, \mathbf{U}_{h}^{*}), C_{1}\mathsf{c}_{\mathscr{K}}^{1.5}), & \text{if } k = 1, 2 \\ 0, & \text{if } k = 0 \end{cases} \tag{20}$$

for the shallow water equations with

$$\mathscr{R}_{k}^{n}(\mathbf{U}_{h}, \mathbf{U}_{h}^{*}) := \max_{i} \left| \max_{\mathbf{x} \in \mathscr{K}_{k}^{n}} \|\mathbf{V} \cdot \mathscr{F}_{i}(\mathbf{U}_{h})\| \right| + \sum_{\mathscr{S}_{m} \subset \partial \mathscr{K}_{k}^{n}} \frac{C_{0}}{\mathsf{c}_{\mathscr{K}}} \max_{i} \left| \max_{\mathbf{x} \in \mathscr{S}_{m}} \|[\![\mathscr{F}_{i}]\!]\| \right|, \tag{21}$$

$\mathsf{c}_{\mathscr{K}} = \min(\mathsf{c}_{1}, \mathsf{c}_{2})$ a scaling factor, $\max_{\mathbf{x} \in \mathscr{K}_{k}^{n}} \| \cdot \|$ is based on the midpoint of the reference element, $\max_{\mathbf{x} \in \mathscr{S}_{m}} \| \cdot \|$ is based on the midpoint of the face of the reference element, and C_{i} for $i = 0, 1, 2$ and γ are positive constants. The positive constants are taken from [24] as $C_{0} = 1.2$ if the normal of the face $\mathscr{S}_{m}$ is parallel to the time direction or else $C_{0} = 1.0$, $C_{1} = 0.1$, $C_{2} = 0.1$ to 1.0 and $\gamma = 0.1$ in which C_{2} is tuned depending upon the desired quality of solution.

Krivodonova et al. [9] proposed a discontinuity detector scheme, to apply numerical dissipation (17) only near discontinuities. We adopt the Krivodonova discontinuity detector for the shallow water equations as follows:

$$\mathscr{I}_{k}^{n}(h_{h}, h_{h}^{*}) := \frac{\sum_{\mathscr{S}_{m} \in \partial \mathscr{K}_{k}^{n}} \int_{\mathscr{S}_{m}} |h^{+} - h^{-}| \, \mathrm{d}\mathscr{S}}{\mathsf{h}_{\mathscr{K}}^{(p+1)/2} |\partial \mathscr{K}_{k}^{n}| \max \|h_{h}\|}, \tag{22}$$

where h_{h} is the approximated water depth, $\mathsf{h}_{\mathscr{K}}$ the cell measure defined as the radius of the largest circumscribed circle in the element $\mathscr{K}_{k}^{n}$, $|\partial \mathscr{K}_{k}^{n}|$ the surface area of the element, and $\max \| \cdot \|$ the maximum norm based on local Gauss' integration points in the element $\mathscr{K}_{k}^{n}$. Now the space–time elements in non-smooth and smooth regions are detected by $\mathscr{I}_{k}^{n} > 1$ and $\mathscr{I}_{k}^{n} < 1$, respectively. The weak formulation (15) is combined with the dissipation operator (17) based on the discontinuity detector (22) by adding the term $\Theta(\mathscr{I}_{k}^{n} - 1)\mathfrak{D}_{k}^{n}(\mathbf{U}_{h}, \mathbf{U}_{h}^{*})$ to (15), where $\Theta(\mathscr{I}_{k}^{n} - 1)$ is the Heaviside function.

3.4. Numerical HLLC flux

In the weak formulation (15), we introduced the approximate numerical flux $\widehat{\widetilde{\mathscr{F}}}(\mathbf{U}^{l}, \mathbf{U}^{r}, \mathbf{n}_{\mathscr{K}})$ because the solution vector $\mathbf{U}_{h}$ is discontinuous at the element face, as in Fig. 2. The numerical flux is usually given by the solution of the Riemann problem identified with the trace values $\mathbf{U}^{l,r}$ directly on either side of the face. Since the solution of Riemann problem is computationally expensive, approximate Riemann solvers
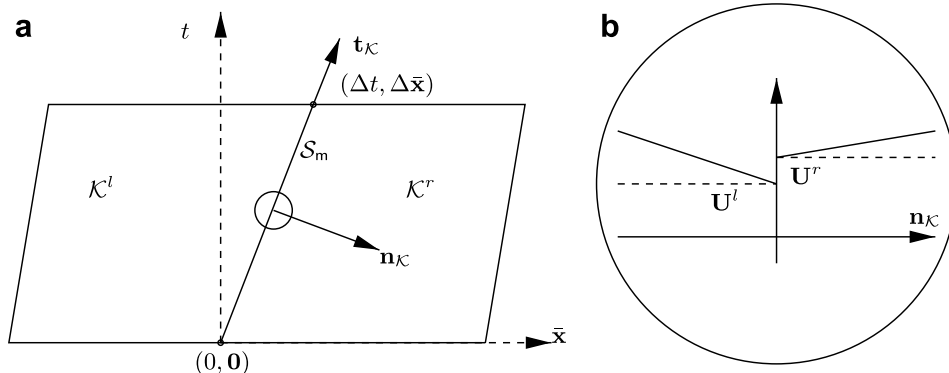

Fig. 2. (a) Geometry at a face $\mathscr{S}_{m}$ connecting the space–time elements $\mathscr{K}^{l}$ and $\mathscr{K}^{r}$. (b) Local Riemann problem at a face.

are used in practice. The HLLC solver in [23] is such an efficient and approximate Riemann solver. In [4], the HLLC solver was improved with appropriate choices of acoustic and contact wave velocities for the Euler equations. Further in [24], this solver was extended to dynamic grids. We show here that the HLLC flux can be derived in space–time without making any explicit difference between space and time such that the resulting flux is applicable at all the faces of the space–time element. The approach applies the HLLC-technique in pseudo-time τ and the direction χ of the outward normal in a space–time element.

To analyze the HLLC flux through the face $\mathscr{S}_{\mathrm{m}}$, we first have to understand the geometry at the face $\mathscr{S}_{\mathrm{m}}$ connecting the space–time elements $\mathscr{K}^{\mathrm{l}}$ and $\mathscr{K}^{\mathrm{r}}$. For convenience, let us take the coordinate axis with the origin located at the bottom corner of the face $\mathscr{S}_{\mathrm{m}}$ as in Fig. 2(a). Now, the top corner of the face $\mathscr{S}_{\mathrm{m}}$ can be taken $(\Delta t, \Delta \bar{\mathbf{x}})$ with $\Delta \bar{\mathbf{x}} = (\Delta x, \Delta y)$ the displacement of the top corner from the bottom corner in the x and y directions, respectively. The tangential vector $\mathbf{t}_{\mathscr{K}}$ along the face can be taken as $(\Delta t, \Delta \bar{\mathbf{x}})^{\mathrm{T}}$. Since the tangential and normal vectors are orthogonal, we have

$$n_t = -\bar{\mathbf{n}}_{\mathscr{K}} \cdot \Delta \bar{\mathbf{x}} \big/ \Delta t = -\bar{\mathbf{n}}_{\mathscr{K}} \cdot \mathbf{v}_g = -v_g \big/ \sqrt{1 + v_g^2} \tag{23}$$

with $\mathbf{n}_{\mathscr{K}} = (n_t, \bar{\mathbf{n}}_{\mathscr{K}})$ the unit space–time normal vector of the face $\mathscr{S}_{\mathrm{m}}$, $\bar{\mathbf{n}}_{\mathscr{K}} = (n_x, n_y) = (\tilde{n}_x, \tilde{n}_y) \big/ \sqrt{1 + v_g^2}$, $\tilde{\mathbf{n}}_{\mathscr{K}} = (\tilde{n}_x, \tilde{n}_y)$ the spatial normal vector, $\mathbf{v}_g = \Delta \bar{\mathbf{x}} / \Delta t$ the grid velocity and $v_g = \tilde{\mathbf{n}}_{\mathscr{K}} \cdot \mathbf{v}_g$ the normal grid velocity. To unify the derivation of a space–time numerical flux, we consider the one-dimensional shallow water equations in the direction $\mathbf{n}_{\mathscr{K}}$ normal to a space–time face of an element. By ignoring dependencies in the other directions, we obtain

$$\partial_\tau \mathbf{U} + \partial_\chi \widehat{\mathbf{F}} = 0 \tag{24}$$

with $\mathbf{U} = (h, hu, hv)^{\mathrm{T}}$, $\widehat{\mathbf{F}} = (hq, huq + n_x P, hvq + n_y P)^{\mathrm{T}}$, effective pressure $P = gh^2/2$, space–time velocity

$$q = n_t + \bar{n}_{\mathscr{K}} \cdot \mathbf{u}, \tag{25}$$

χ the coordinate in the direction of $\mathbf{n}_{\mathscr{K}}$, and pseudo-time τ. The spatial HLLC approach of [4] is now applied to (24) but in the τ, χ-space. The HLLC wave patterns are sketched in Fig. 3(a) in the physical $t, \bar{\mathbf{x}}$-space and in Fig. 3(b) in the τ, χ-space. In physical space, the left and right waves are taken as

$$S_1 = \min(\tilde{q}_1 - a_1, \tilde{q}_{\mathrm{r}} - a_{\mathrm{r}}) \quad \text{and} \quad S_{\mathrm{r}} = \max(\tilde{q}_1 + a_1, \tilde{q}_{\mathrm{r}} + a_{\mathrm{r}}) \tag{26}$$

with $\tilde{q} = \tilde{\mathbf{n}}_{\mathscr{K}} \cdot \mathbf{u}$ the speed in the spatial normal direction, as in [4], and $a^2 = \partial P / \partial h$. We infer from (25) that

$$s_{\mathrm{r}} = (S_{\mathrm{r}} - v_g) \big/ \sqrt{1 + v_g^2} \quad \text{and} \quad s_{\mathrm{r}} = (S_1 - v_g) \big/ \sqrt{1 + v_g^2}. \tag{27}$$

As usual, four possible cases occur (i) $s_1 < 0, s_{\mathrm{r}} > 0, s_m > 0$; (ii) $s_1 < 0, s_{\mathrm{r}} > 0, s_m < 0$; (iii) $s_1 < 0, s_{\mathrm{r}} < 0, s_m < 0$ and (iv) $s_1 > 0, s_{\mathrm{r}} > 0, s_m > 0$. Combining the HLLC flux for the four cases (as in [4]), but in the τ, χ-space, we obtain

$$\widehat{\mathbf{F}}_{\mathrm{HLLC}}(\mathbf{U}^{\mathrm{l}}, \mathbf{U}^{\mathrm{r}}, \mathbf{n}_{\mathscr{K}}) = \frac{1}{2}\{\widehat{\mathbf{F}}^{\mathrm{l}} + \widehat{\mathbf{F}}^{\mathrm{r}} - (|s_1| - |s_m|)\mathbf{U}^{*\mathrm{l}} + (|s_{\mathrm{r}}| - |s_m|)\mathbf{U}^{*\mathrm{r}} + |s_1|\mathbf{U}^{\mathrm{l}} - |s_{\mathrm{r}}|\mathbf{U}^{\mathrm{r}}\}, \tag{28}$$

where $\widehat{\mathbf{F}}^{\mathrm{l,r}} = \widehat{\mathbf{F}}(\mathbf{U}^{\mathrm{l,r}})$. The usual HLLC-expressions for the wave speed s_m and the average intermediate states $\mathbf{U}^{*\mathrm{l}}$ and $\mathbf{U}^{*\mathrm{r}}$ are given next.
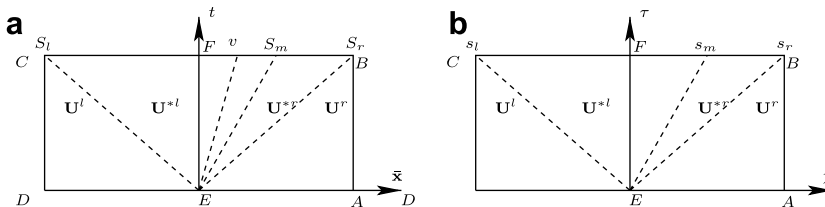

Fig. 3. (a) HLLC wave pattern in physical space with $v_g = \bar{\mathbf{n}}_{\mathscr{K}} \cdot \mathbf{v}_g$. (b) The HLLC pattern in τ, χ-space.

As in [4] we assume $s_m = q_1^* = q_r^* = q^*$ where q^* is the average directed velocity between the left and right waves. The q^* can be obtained from the average intermediate state $\mathbf{U}^*$ calculated using HLL approach (see Fig. 4). The average intermediate state $\mathbf{U}^*$ is given by

$$\mathbf{U}^* = (s_r \mathbf{U}^r - s_1 \mathbf{U}_1 - (\hat{\mathbf{F}}^r - \hat{\mathbf{F}}^l))/(s_r - s_1). \tag{29}$$

The wave speed s_m follows from (29) as

$$s_m = q^* = \frac{\mathbf{n}_\mathscr{K} \cdot \mathbf{U}^*}{h^*} = \frac{h_r q_r(s_r - q_r) - h_1 q_1(s_1 - q_1) - (n_x^2 + n_y^2)(P_r - P_1)}{h_r(s_r - q_r) - h_1(s_1 - q_1)} \tag{30}$$

with h^* the average intermediate depth, following from (29). By substituting the expressions (25) and (27) into (30), it follows that $s_m = (S_m - v_g)/\sqrt{1 + v_g^2}$, as expected heuristically. Here S_m is the expression in [4]; essentially it follows by replacing the space–time variables in (30) by their space counterparts as in: $s_m \to S_m$, $s_r \to S_r$, $S_1 \to s_1$, $q_1 \to \tilde{q}_1$ and $q_r \to \tilde{q}_r$.

The intermediate states U^{*l} and U^{*r} are determined by using the Rankine–Hugonoit relations across left wave and right wave as

$$(s_{l,r} - s_m)\mathbf{U}^{*l,*r} = (s_{l,r} - q_{l,r})\mathbf{U}^{l,r} + (\hat{\mathbf{P}}^{*l,*r} - \hat{\mathbf{P}}^{l,r}), \tag{31}$$

where $\hat{\mathbf{P}}^{*l,*r} = (0, n_x P_{l,r}^*, n_y P_{l,r}^*)$ is the average intermediate normal pressure, $P_{l,r}^*$ is the average intermediate pressure obtained by multiplying (31) with $\mathbf{n}_\mathscr{K}$ and is given by

$$P^* = P_{l,r}^* = P_{l,r} + (h_{l,r}(s_{l,r} - q_{l,r})(s_m - q_{l,r}))/(n_x^2 + n_y^2). \tag{32}$$

When $s_1 > 0$ the flux simplifies to $\hat{\mathbf{F}}_1$ and when $s_r < 0$ to $\hat{\mathbf{F}}_r$, i.e. the classic upwind cases.

The expressions (27)–(32) for our HLLC flux, using

$$\mathbf{n}_\mathscr{K} = (n_t, n_x, n_y) = (-v_g, \tilde{n}_x, \tilde{n}_y)\Big/\sqrt{1 + v_g^2} \tag{33}$$

reduce to the expressions in [24]: in comparison our flux is multiplied by a factor $1/\sqrt{1 + v_g^2}$ because we included the space–time normal. In the limit $v_g \to \infty$, we obtain

$$\hat{\mathbf{F}}_{HLLC} = \lim_{v_g \to \infty} \hat{\mathbf{F}}_r = -(h_r, u_r, u_r, h_r v_r)^T. \tag{34}$$

This is consistent since we are at the bottom face $t = t_n$ of a space–time element with space–time normal $\mathbf{n}_\mathscr{K} = (-1, 0, 0)^T$, and (24) becomes $\partial_\tau \mathbf{U} - \partial_\chi \mathbf{U} = 0$. Causality in time thus reduces to an upwind flux in our unified approach, as expected. Likewise, we find at the top $t = t_{n+1}$ of the space–time element that $v_g \to -\infty$

$$\hat{\mathbf{F}}_{HLLC} = \lim_{v_g \to -\infty} \hat{\mathbf{F}}_1 = (h_1, u_1, u_1, h_1 v_1)^T, \tag{35}$$

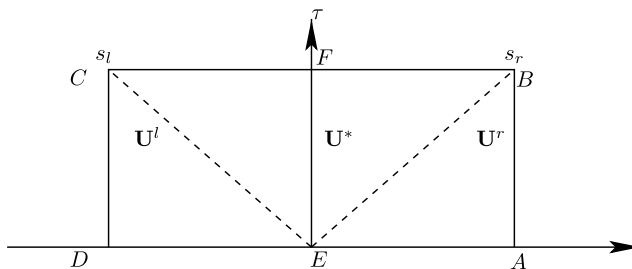and (24) becomes $\partial_\tau \mathbf{U} + \partial_\chi \mathbf{U} = 0$.

Fig. 4. Riemann fan for shallow water equations (HLL approach).

3.5. Discretized weak formulation: non-linear equations

The weak formulation (15) is discretized by substituting the polynomial approximation of the state vector $\mathbf{U}_h$ and using the arbitrariness of the test function $\mathbf{W}_h$ as $(\psi_j, 0, 0)$, $(0, \psi_j, 0)$ and $(0, 0, \psi_j)$, $j = 0, \ldots, M - 1$ with $M = 5$ or $M = 8$. The discretized equations can now be obtained as

$$L_{k;ij}^{n;\mathscr{K}}(\widehat{\mathbf{U}}^n; \widehat{\mathbf{U}}^{n-1}) = \sum_{\mathscr{S}_m \subset \partial \mathscr{K}_k^n} F_{m;ij}^{k;\mathscr{S}} - E_{k;ij}^{n;\mathscr{K}} + \Theta(\mathscr{I}_k^n - 1) D_{k;ij}^{n;\mathscr{K}} - G_{k;ij}^{n;\mathscr{K}} = 0, \tag{36}$$

where $i = 0, 1, 2$ is the index for the shallow water equations, m the index for the expansion coefficients, m the index for the faces and k the index for the elements. The various terms in the non-linear equations (36) are represented as follows:

$$E_{k;ij}^{n;\mathscr{K}}(\widehat{\mathbf{U}}^n) = \int_{\mathscr{K}_k^n} \nabla \psi_j \cdot \mathscr{F}_i(\mathbf{U}_h) \, d\mathscr{K},$$

$$F_{m;ij}^{k;\mathscr{S}}(\widehat{\mathbf{U}}^n, \widehat{\mathbf{U}}^{n-1}) = \int_{\mathscr{S}_m \subset \partial \mathscr{K}_k^n} \widehat{F}_i(\mathbf{U}^l, \mathbf{U}^r, \mathbf{n}_{\mathscr{K}}) \psi_j \, d\mathscr{S}, \quad \mathsf{k} = l \text{ or } r$$

$$D_{k;ij}^{n;\mathscr{K}}(\widehat{\mathbf{U}}^n, \widehat{\mathbf{U}}^{n-1}) = \sum_{m=0}^{M-1} \widehat{U}_{im}^n \bar{D}_{k;jm}^{n;\mathscr{K}}(\widehat{\mathbf{U}}^n, \widehat{\mathbf{U}}^{n-1}) \quad \text{with} \tag{37}$$

$$\bar{D}_{k;jm}^{n;\mathscr{K}}(\widehat{\mathbf{U}}^n, \widehat{\mathbf{U}}^{n-1}) = \int_{\mathscr{K}_k^n} (\nabla \psi_m)^{\mathrm{T}} \mathfrak{D}_k^n(\mathbf{U}_h, \mathbf{U}_h^*)(\nabla \psi_j) \, d\mathscr{K}, \quad \text{and}$$

$$G_{k;ij}^{n;\mathscr{K}}(\widehat{\mathbf{U}}^n) = \int_{\mathscr{K}_k^n} \psi_j S_i \, d\mathscr{K}.$$

Given the coefficients $\widehat{\mathbf{U}}^{n-1}$ at the previous time level t_{n-1}, we have to find the coefficients $\widehat{\mathbf{U}}^n$ satisfying (36) at the present time level t_n.

3.6. Pseudo-time integration: non-linear solver

To solve the system of non-linear equations (36) obtained from the space–time discontinuous Galerkin discretization, we augment these equations with a pseudo-time derivative as

$$|K_k^n| \frac{\partial \widehat{U}_{ij}}{\partial \tau} = -\frac{1}{\Delta t} L_{k;ij}^{n;\mathscr{K}}(\widehat{\mathbf{U}}; \widehat{\mathbf{U}}^{n-1}) \tag{38}$$

with $\Delta t = (t_n - t_{n-1})$ the time step and $|K_k^n| = |\mathscr{K}_k^n|/\Delta t$. Now we integrate (38) until the solution reaches steady state in pseudo-time, i.e., $L_{k;ij}^{n;\mathscr{K}}(\widehat{\mathbf{U}}^n; \widehat{\mathbf{U}}^{n-1}) \approx 0$. The pseudo-time integration is performed by using a second-order accurate five-stage Runge–Kutta scheme as described in Ambati and Bokhove [2]. The pseudo-time step $\Delta \tau$ is determined locally per space–time element by a CFL condition given as $\Delta \tau|_{\mathscr{K}_k^n} = \mathrm{CFL}_{\Delta \tau} |K_k^n|/S_{k;max}^n$ with $S_{k;max}^n$ the maximum wave speed in the space–time element $\mathscr{K}_k^n$ and $\mathrm{CFL}_{\Delta \tau} = 0.8$ the CFL number for the pseudo-time step.

4. Properties and analysis of the numerical discretization

4.1. Persistence of the discretized rest state

The shallow water equations at rest satisfy $\mathbf{u} = 0$ for a fixed depth $h(\mathbf{x}) = D(\bar{\mathbf{x}})$ such that $\overline{\nabla}(gh^2/2) = -gh\overline{\nabla}h_b$. For smooth topography $h_b(\bar{\mathbf{x}}) + h(\mathbf{x}) = H$ is constant.

Proposition 3. Consider the shallow water equations with a consistent and conservative numerical flux $\widehat{\mathbf{F}}(\mathbf{U}^-, \mathbf{U}^+, \mathbf{n}_{\mathscr{K}})$ and the weak formulation (15). The weak formulation (15) exactly satisfies the steady rest state $\mathbf{u} = 0$, $H = h(\mathbf{x}) + h_b(\bar{\mathbf{x}})$ if

(1) The bottom topography $h_b(\bar{\mathbf{x}})$ is approximated smoothly as follows:

$$\tilde{h}_b(\bar{\mathbf{x}}) = \sum_0^{M-1} \hat{h}_{b;m} \psi_m \quad \text{such that} \tag{39}$$

$$h_b(x_k, y_k) = \tilde{h}_b(x_k, y_k) \quad \text{for } k = 0, 1, 2 \text{ and } 3 \tag{40}$$

with $\tilde{h}_b(\bar{\mathbf{x}})$ the approximated topography, ψ_m the basis functions, $\hat{h}_{b;m}$ the expansion coefficients of the topographic approximation and (x_k, y_k) the nodal coordinates of the spatial element K_k. The expansion coefficients corresponding to the time coordinate are taken zero.

(2) The rest water depth $h(\mathbf{x})$ is approximated as

$$\tilde{h}(\bar{\mathbf{x}}) = H - \tilde{h}_b(\bar{\mathbf{x}}) = \sum_{m=0}^{M-1} \hat{h}_m \psi_m \tag{41}$$

with $\tilde{h}(\bar{\mathbf{x}})$ the approximated water depth and $\hat{h}_m$ the expansion coefficient of the water depth obtained using a (dis)continuous Galerkin projection with expansion coefficients corresponding to time set to zero.

(3) The spatial element K_k^n is not deforming in time.

Proof. We give the proof for the case with $M = 5$. The approximated topography $\tilde{h}_b(\bar{\mathbf{x}})$ as given in (39) satisfying (40) ensures that $\tilde{h}_b(\bar{\mathbf{x}})$ is piecewise continuous and linear along the faces. Hence, $\tilde{h}$ in (41) is also piecewise continuous and linear along the faces. Since the velocities are zero, we can now conclude that $\mathbf{U}_h = (\tilde{h}, \tilde{h}u, \tilde{h}v)$ is piecewise continuous and linear along the faces. Also the traces on each element boundary from the inside and outside the element are equal, i.e., $\mathbf{U}_h|_{\partial\mathscr{K}_k^n} = \mathbf{U}^- = \mathbf{U}^+$. Using the consistency property of numerical flux, we get

$$\widetilde{\mathscr{F}}(\mathbf{U}^-, \mathbf{U}^+, \mathbf{n}_\mathscr{K}) = \mathscr{F}(\mathbf{U}_h). \tag{42}$$

Substituting (42) in (15) for every element, we obtain an alternative form of the weak formulation as follows:

$$\int_{\partial\mathscr{K}_k^n} W_j^- (\mathbf{n}_\mathscr{K} \cdot \mathscr{F}_i(U_h)) \, d(\partial\mathscr{K}) - \int_{\mathscr{K}_k^n} \boldsymbol{\nabla} W_{hj} \cdot \mathscr{F}_i(U_h) \, d\mathscr{K} - \int_{\mathscr{K}_k^n} W_{hj} S_i \, d\mathscr{K} = 0. \tag{43}$$

After integrating by parts and applying Gauss' theorem in space and time, we get

$$\int_{\mathscr{K}_k^n} W_{hi} (\nabla \cdot \mathscr{F}_i(\mathbf{U}_h)) \, d\mathscr{K} - \int_{\mathscr{K}_k^n} W_{hi} S_i \, d\mathscr{K} = 0. \tag{44}$$

Since $\mathbf{W}_h$ is arbitrary, the approximation $\mathbf{U}_h$ needs to satisfy

$$\nabla \cdot \mathscr{F}_i(\mathbf{U}_h) = S_i. \tag{45}$$

Substituting the approximations $\mathbf{U}_h$ in $\nabla \cdot \mathscr{F}_i(\mathbf{U}_h)$, we get

$$\partial_t \tilde{h} = \partial_t(H - \tilde{h}_b) = 0, \quad \text{and} \quad \overline{\nabla}(g\tilde{h}^2/2) = g\tilde{h}\overline{\nabla}(H - \tilde{h}_b) = -g\tilde{h}\overline{\nabla}\tilde{h}_b. \tag{46}$$

Hence, the steady rest state is satisfied in the discretized equations. □

This strategy to preserve the rest state coincides with the one in [5,21], and contrasts with the ones in [3,10], because we consider smooth topography. Preservation of the rest state with discontinuous bottom topography and a Galerkin finite element method is found in Rhebergen et al. [18].

4.2. Discrete Fourier analysis of the numerical discretization

For the discrete Fourier analysis of the space–time DG discretization, we consider the one-dimensional linearized rotating shallow water equations

$$\partial_t \eta + \partial_x(Hu) = 0, \quad \partial_t u - fv = -g\partial_x \eta \quad \text{and} \quad \partial_t v + fu = 0 \tag{47}$$

with $\eta(t,x)$ the free surface perturbation around a mean surface depth H, $(u(t,x), v(t,x))$ the velocity field, g the gravitational acceleration and f the Coriolis parameter.

These equations can be solved using the following ansatz:

$$\eta(t,x) = A e^{\iota(kx+\omega t)} \quad \text{and} \quad (u(t,x), v(t,x)) = \frac{-gAk}{(\omega^2 - f^2)}(\omega, f\iota) e^{\iota(kx+\omega t)} \tag{48}$$

yielding the dispersion relation $\omega^2 = a^2 k^2 + f^2$ with amplitude A, frequency ω, wave number k and gravity wave speed $a = \sqrt{gH}$.

To discretize (47), we consider one-dimensional space–time elements $\mathscr{K}_k^n$ with neighboring elements $\mathscr{K}_{k-1}^n$ and $\mathscr{K}_{k+1}^n$ in the x-direction, and $\mathscr{K}_k^{n-1}$ and $\mathscr{K}_k^{n+1}$ in the t-direction. The faces of the space–time element $\mathscr{K}_k^n$ can now be given by $\mathscr{S}_1 = \overline{\mathscr{K}_{k-1}^n} \cap \overline{\mathscr{K}_k^n}, \mathscr{S}_r = \overline{\mathscr{K}_k^n} \cap \overline{\mathscr{K}_{k+1}^n}, \mathscr{S}_b = \overline{\mathscr{K}_k^{n-1}} \cap \overline{\mathscr{K}_k^n}$ and $\mathscr{S}_t = \overline{\mathscr{K}_k^n} \cap \overline{\mathscr{K}_k^{n+1}}$ with element boundary $\partial \mathscr{K}_k^n = \mathscr{S}_1 \cup \mathscr{S}_r \cup \mathscr{S}_b \cup \mathscr{S}_t$. In each space–time element, we approximate the wave field (η, u, v) as

$$(\eta_k^n, u_k^n, v_k^n) = \sum_{j=0}^{2} (\hat{\eta}_{k,j}^n, \hat{u}_{k,j}^n, \hat{v}_{k,j}^n) \psi_j \tag{49}$$

with $(\hat{\eta}_{k,j}^n, \hat{u}_{k,j}^n, \hat{v}_{k,j}^n)$ the expansion coefficients and ψ_j the basis functions. The basis functions ψ_j in the reference elements $\hat{\mathscr{K}}$ are defined as $\hat{\psi} = (1, \zeta_0 - 1, \zeta)$.

To simplify the weak formulation (15) per space–time element, we substitute $(\tilde{\eta}, \tilde{u}, \tilde{v}) := (\eta^+, u^-, v^-)$ in the numerical flux evaluation at the elements faces $\mathscr{S}_1$ and $\mathscr{S}_r$, and the upwind flux in the time direction. The weak formulation (37) then becomes

$$-\int_{\mathscr{S}_b} \eta_k^{n-1} w_1^- \, d\mathscr{S} + \int_{\mathscr{S}_t} \eta_k^n w_1^- \, d\mathscr{S} - \int_{\mathscr{S}_1} H u_{k-1}^n w_1^- \, d\mathscr{S} + \int_{\mathscr{S}_r} H u_k^n w_1^- \, d\mathscr{S}$$

$$- \int_{\mathscr{K}_k^n} (\partial_t w_1) \eta_k^n \, d\mathscr{K} - \int_{\mathscr{K}_k^n} (\partial_x w_1) H u_k^n \, d\mathscr{K} = 0,$$

$$-\int_{\mathscr{S}_b} u_k^{n-1} w_2^- \, d\mathscr{S} + \int_{\mathscr{S}_t} u_k^n w_2^- \, d\mathscr{S} - \int_{\mathscr{S}_1} g \eta_k^n w_2^- \, d\mathscr{S} + \int_{\mathscr{S}_r} g \eta_{k+1}^n w_2^- \, d\mathscr{S} \tag{50}$$

$$- \int_{\mathscr{K}_k^n} (\partial_t w_2) u_k^n \, d\mathscr{K} - \int_{\mathscr{K}_k^n} (\partial_x w_2) g \eta_k^n \, d\mathscr{K} - \int_{\mathscr{K}_k^n} w_2 f v_k^n \, d\mathscr{K} = 0,$$

$$-\int_{\mathscr{S}_b} v_k^{n-1} w_3^- \, d\mathscr{S} + \int_{\mathscr{S}_t} v_k^n w_3^- \, d\mathscr{S} - \int_{\mathscr{K}_k^n} (\partial_t w_3) v_k^n \, d\mathscr{K} + \int_{\mathscr{K}_k^n} w_3 f u_k^n \, d\mathscr{K} = 0$$

with (w_1, w_2, w_3) the test functions. Substituting the polynomial approximation (49) in (50), the numerical discretization is obtained as

$$-A_k^n \hat{\eta}_k^{n-1} + B_k^n \hat{\eta}_k^n - H C_k^{n,1} \hat{u}_{k-1}^n + H D_k^{n,1} \hat{u}_k^n - E_k^n \hat{\eta}_k^n - H F_k^n \hat{u}_k^n = 0,$$

$$-A_k^n \hat{u}_k^{n-1} + B_k^n \hat{u}_k^n - g C_k^{n,2} \hat{\eta}_k^n + g D_k^{n,2} \hat{\eta}_{k+1}^n - E_k^n \hat{u}_k^n - g F_k^n \hat{\eta}_k^n - f G_k^n \hat{v}_k^n = 0, \tag{51}$$

$$-A_k^n \hat{v}_k^{n-1} + B_k^n \hat{v}_k^n - E_k^n \hat{v}_k^n + f G_k^n \hat{u}_k^n = 0,$$

where the 3×3 matrices are defined as follows:

$$A_{k;ij}^n := \int_{\mathscr{S}_b} \psi_j^+ \psi_i^- \, d\mathscr{S}, \quad B_{k;ij}^n := \int_{\mathscr{S}_t} \psi_j^- \psi_i^- \, d\mathscr{S}, \quad C_{k;ij}^{n,1} := \int_{\mathscr{S}_1} \psi_j^+ \psi_i^- \, d\mathscr{S},$$

$$C_{k;ij}^{n,2} := \int_{\mathscr{S}_1} \psi_j^- \psi_i^- \, d\mathscr{S}, \quad D_{k;ij}^{n,1} := \int_{\mathscr{S}_r} \psi_j^- \psi_i^- \, d\mathscr{S}, \quad D_{k;ij}^{n,2} := \int_{\mathscr{S}_r} \psi_j^+ \psi_i^- \, d\mathscr{S}, \tag{52}$$

$$E_{k;ij}^n := \int_{\mathscr{K}_k^n} \psi_j (\partial_t \psi_i) \, d\mathscr{K}, \quad F_{k;ij}^n := \int_{\mathscr{K}_k^n} \psi_j (\partial_x \psi_i) \, d\mathscr{K} \quad \text{and} \quad G_{k;ij}^n := \int_{\mathscr{K}_k^n} \psi_j \psi_i \, d\mathscr{K}.$$

To investigate the stability, dispersion and dissipation error of the numerical scheme, we use a discrete Fourier ansatz for the coefficients of the wave field as

$$(\hat{\eta}_k^n, \hat{u}_k^n, \hat{v}_k^n) := \lambda^n \exp(\iota k k \Delta x)(\hat{\eta}_F, \hat{u}_F, \hat{v}_F), \tag{53}$$

where $(\hat{\eta}_F, \hat{u}_F, \hat{v}_F)$ are the Fourier coefficients.

Substituting (53) into the discretized equations (51), we obtain

$$
\begin{aligned}
& M_k^n \hat{\eta}_F + \lambda H(-\exp(-\iota k \Delta x) C_k^{n,1} + D_k^{n,1} - F_k^n) \hat{u}_F = 0, \\
& M_k^n \hat{u}_F + \lambda g(-C_k^{n,2} + \exp(\iota k \Delta x) D_k^{n,2} - F_k^n) \hat{\eta}_F - \lambda f G_k^n \hat{v}_F = 0, \\
& M_k^n \hat{v}_F + \lambda f G_k^n \hat{u}_F = 0
\end{aligned}
\tag{54}
$$

with $M_k^n = -A_k^n + \lambda B_k^n - \lambda E_k^n$. Combining Eqs. (54), we get the following eigenvalue problem:

$$\left[M_k^n + f^2 G_k^n (M_k^n)^{-1} G_k^n - (\lambda a)^2 H_k^{n,1} (M_k^n)^{-1} H_k^{n,2} \right] \hat{u}_F = 0 \tag{55}$$

with $H_k^{n,1} = -\exp(-\iota k \Delta x) C_k^{n,1} + D_k^{n,1} - F_k^n$ and $H_k^{n,2} = -C_k^{n,2} + \exp(\iota k \Delta x) D_k^{n,2} - F_k^n$. If we take uniform elements of size Δx and Δt then we find using XMAPLE that $(M_k^n)^{-1}$ is of the form $M_1/(\lambda - 1) + M_2/(\lambda)$. After some algebraic manipulations, a simplified quadratic eigenvalue problem can be obtained of the following form:

$$\lambda^2 P + \lambda Q + R = 0. \tag{56}$$

Using MATLAB, we solve for the eigenvalues λ with $k \Delta x = [0, 2\pi]$, the CFL number $\mathrm{CFL}_{\Delta t} = a \Delta t / \Delta x$ and Coriolis parameter f. For a wide range of CFL numbers and Coriolis parameters, we always obtained $\max |\lambda| < 1$, which shows that the scheme is unconditionally stable.

The eigenvalue λ is analogous to the frequency of the harmonic wave as

$$\lambda = \exp(\iota \tilde{\omega} \Delta t) \tag{57}$$

with $\tilde{\omega} = \tilde{\omega}_1 + \iota \tilde{\omega}_2$ in which $\tilde{\omega}_1$ is the numerical frequency and $\tilde{\omega}_2$ is the dissipation of the numerical scheme. The dispersion error $|\tilde{\omega}_1 - \omega|$ and dissipation error $\tilde{\omega}_2$ of the numerical scheme can now be given as

$$|\tilde{\omega}_1 - \omega| = |\arg(\lambda) - \omega| \quad \text{and} \quad \tilde{\omega}_2 = -\frac{\ln(|\lambda|)}{\Delta t}, \tag{58}$$

respectively. Some of the eigenvalues of (56) will be close to the actual frequencies of the harmonic wave, which we use to compute the dispersion error and dissipation of the numerical scheme. In Figs. 5–7, we have plotted the contours of dispersion and dissipation errors for mesh resolution $k \Delta x = [0, 0.25]$, wave frequency resolution $\Omega \Delta t = [0, 0.25]$, Coriolis parameter $f = 0, 2, 3$ and wave number $k = 1$. We can observe from the plots that the dispersion error and dissipation error decrease with the increase of the mesh resolution and the wave frequency resolution. The exact and numerical dispersion relations in Fig. 8 reveal the dispersion error in another way.
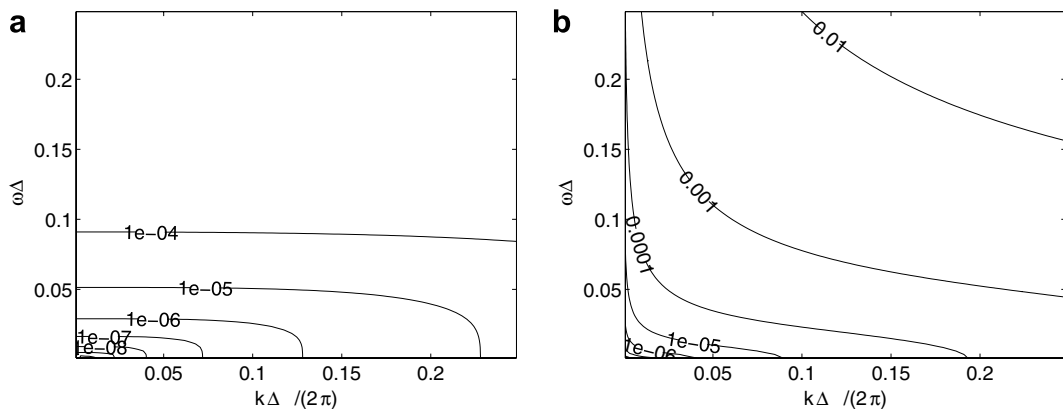

Fig. 5. $f = 0$, $ak = 1$ and $f^2 < a^2 k^2$. (a) Dispersion error and (b) dissipation error.
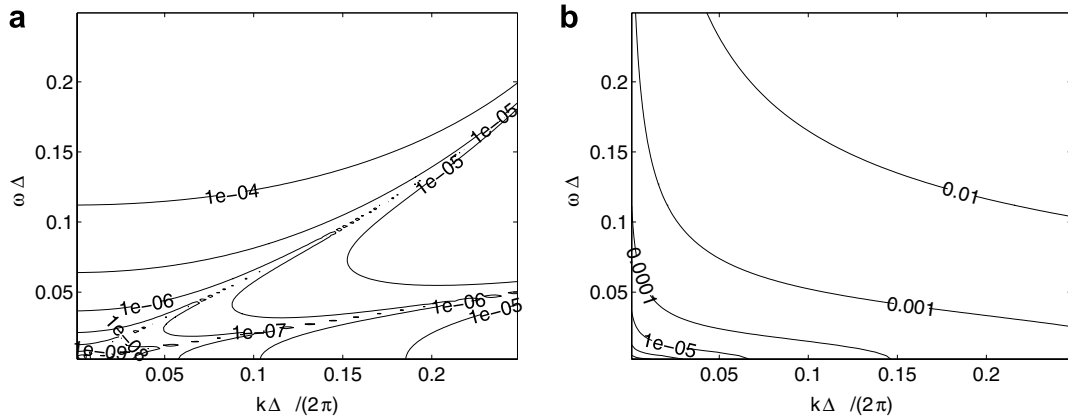
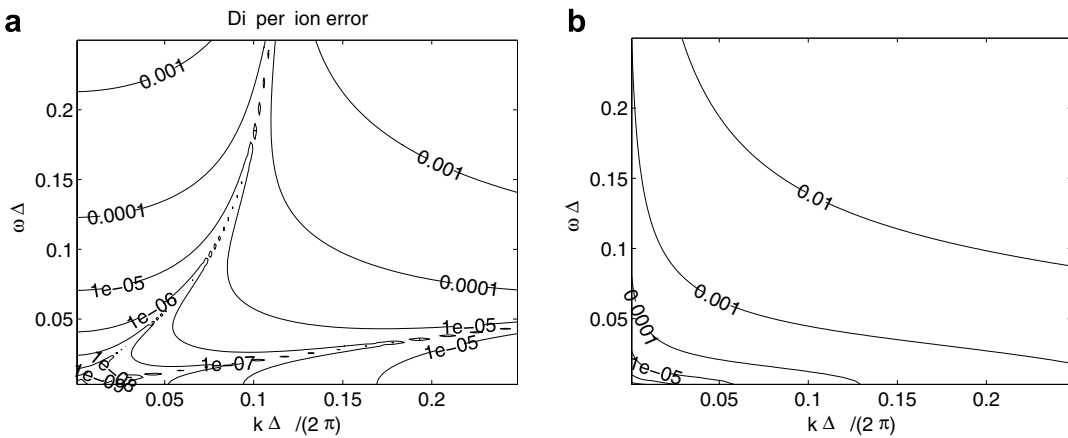Fig. 6. $f = 2$, $ak = 1$ and $f^2 > a^2k^2$. (a) Dispersion error and (b) dissipation error.

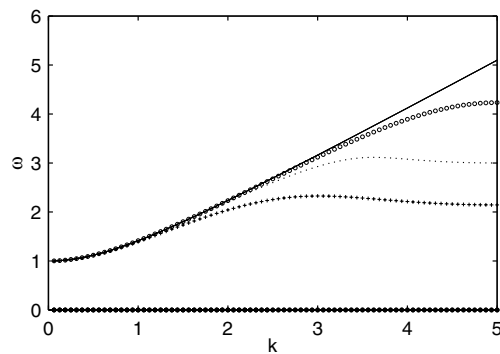Fig. 7. $f = 3$, $ak = 1$ and $f^2 > a^2k^2$. (a) Dispersion error and (b) dissipation error.

Fig. 8. Plot of numerical and actual frequencies for different wave numbers k with mesh size $\Delta x = 2\pi/10$ and $f = 1$. Solid lines correspond to the actual frequency ω and the marks "+", "." and "○" correspond to the numerical frequencies $\tilde{\omega}_1$ for $\Delta t = 1.0$, 0.5 and 0.05, respectively.

5. Verification

The space–time discontinuous Galerkin scheme is verified by comparing the numerical results against some exact solutions. Also, the dispersion and dissipation error of the scheme are qualitatively verified for a number

of harmonic waves in rectangular and circular domains. In all the numerical experiments, we work with non-dimensionalized shallow water equations as stated in Section 2. Errors of the numerical results include the $L^2(\Omega_h)$ and $L^\infty(\Omega_h)$ norms

$$\|\text{Error}\|_{L^2(\Omega_h)} := \left(\sum_K \int_{K_k^n} (\mathbf{U}_{\text{exact}} - \mathbf{U}_h)^2 \, \mathrm{d}K \right)^{1/2}, \tag{59}$$

$$\|\text{Error}\|_{L^\infty(\Omega_h)} := \max_K \left(\max_{\mathbf{x} \in K_k^n} \|\mathbf{U}_{\text{exact}} - \mathbf{U}_h\| \right), \tag{60}$$

where the maximum max $\| \cdot \|$ is based on local Gauss integration points within the element K_k^n, and $\mathbf{U}_{\text{exact}}$ and $\mathbf{U}_h$ are exact and numerical solutions, respectively. The order of accuracy ''order'' of the method is obtained as

$$\text{order} = (\ln(\|\text{Error}\|^{(1)}) - \ln(\|\text{Error}\|^{(2)}))/(\ln(h_{\mathscr{K}}^{(1)}) - \ln(h_{\mathscr{K}}^{(2)})), \tag{61}$$

where $\|\text{Error}\|^{(1)}$ and $\|\text{Error}\|^{(2)}$ are the errors computed on the meshes with cell measures $h_{\mathscr{K}}^{(1)}$ and $h_{\mathscr{K}}^{(2)}$, respectively. We have refined the space–time mesh uniformly in both space and time.

For many numerical examples considered here, the implementation of the boundary condition was very crucial in the numerical scheme. To explain the implementation, let $\mathbf{U}^l = (h^l, h^l u^l, h^l v^l)^T$ be the trace taken from inside the element $\mathscr{K}^l$ connected to the boundary face $\mathscr{S}_m \in \Gamma_{\text{bou}}$, $\mathbf{U}^b = (h^b, h^b u^b, h^b v^b)^T$ the boundary data applied at the boundary face $\mathscr{S}_m$ and $\mathbf{n}_{\mathscr{K}}^l = (n_t, \tilde{\mathbf{n}}_{\mathscr{K}})^T$ the outward unit normal vector of the face $\mathscr{S}_m$ w.r.t. element $\mathscr{K}^l$. We have implemented the different boundary conditions given $\mathbf{U}^l$ as follows:

Open flow boundary: At an open flow boundary, we simply take $\mathbf{U}^b = \mathbf{U}^l$.
Solid wall: Consider the momentum equations in primitive variables $\mathbf{u}$ as

$$\partial_t \mathbf{u} + (\mathbf{u} \cdot \nabla)\mathbf{u} = -f\mathbf{u}^\perp - g\nabla(h + h_b) \tag{62}$$

with $\mathbf{u}^\perp = (-v, u)^T$. Taking the dot product of (62) with the normal vector $\bar{\mathbf{n}} = (n_x, n_y)^T$ and using the zero normal velocity $\mathbf{u} \cdot \bar{\mathbf{n}} = 0$ at the wall, we find the following geostrophic balance condition on the resultant tangential velocity component on a linear piece of the boundary:

$$f\mathbf{u} \cdot \bar{\mathbf{t}} = g\bar{\mathbf{n}} \cdot \nabla(h + h_b). \tag{63}$$

When $f = 0$ we find $\bar{\mathbf{n}} \cdot \nabla(h + h_b) = 0$. The velocity is decomposed as follows:

$$\mathbf{u} = (\mathbf{u} \cdot \bar{\mathbf{n}})\bar{\mathbf{n}} + (\mathbf{u} \cdot \bar{\mathbf{t}})\bar{\mathbf{t}} \tag{64}$$

with $\bar{\mathbf{t}} = (-n_y, n_x)$ the tangential vector. For the numerical implementation, we use the ghost value $\mathbf{U}^b$. Rather than using $\mathbf{u} \cdot \bar{\mathbf{n}} = 0$ and $\bar{\mathbf{n}} \cdot \nabla(h + h_b) = 0$ when $f = 0$, we enforce $\mathbf{u}^b \cdot \bar{\mathbf{n}} = -\mathbf{u}^l \cdot \bar{\mathbf{n}}$ and $\mathbf{u}^b \cdot \bar{\mathbf{t}} = \mathbf{u}^l \cdot \bar{\mathbf{t}}$ to obtain

$$h^b = h^l; \quad u^b = (n_y^2 - n_x^2)u^l - 2n_x n_y v^l \quad \text{and} \quad v^b = (n_x^2 - n_y^2)v^l - 2n_x n_y u^l. \tag{65}$$

For $f \neq 0$, the situation appears ambiguous. We took

$$h^b = h^l; \quad (u^b, v^b) = -(u^l, v^l) + (-n_y, n_x)(2g/f)(\bar{\mathbf{n}} \cdot \overline{\nabla}(h + h_b)), \tag{66}$$

such that $\mathbf{u}^b \cdot \bar{\mathbf{n}} = -\mathbf{u}^l \cdot \bar{\mathbf{n}}$ and $\mathbf{u}^b \cdot \bar{\mathbf{t}} = -\mathbf{u}^l \cdot \bar{\mathbf{t}} + 2(g/f)\bar{\mathbf{n}} \cdot \overline{\nabla}(h + h_b)$.
Moving wall: At a moving wall boundary we impose in space–time

$$\mathbf{U}^b \cdot \mathbf{n} = -\mathbf{U}^l \cdot \mathbf{n}, \quad \mathbf{U}^b \cdot \mathbf{t}_1 = \mathbf{U}^l \cdot \mathbf{t}_1 \quad \text{and} \quad \mathbf{U}^b \cdot \mathbf{t}_2 = \mathbf{U}^l \cdot \mathbf{t}_2, \tag{67}$$

where $\mathbf{t}_1$ and $\mathbf{t}_2$ are unit tangential vectors orthogonal to each other and to the normal vector $\boldsymbol{n}$ such that $\mathbf{t}_1 \times \mathbf{t}_2 = \mathbf{n}$. Solving (67) simultaneously and substituting the relation $\mathbf{t}_1 \times \mathbf{t}_2 = \mathbf{n}$, we obtain

$$
\begin{aligned}
h^b &= (-n_t^2 + n_x^2 + n_y^2)h^l - (2n_t n_x)h^l u^l - (2n_t n_y)h^l v^l, \\
h^b u^b &= (-n_x^2 + n_t^2 + n_y^2)h^l u^l - (2n_t n_x)h^l - (2n_x n_y)h^l v^l, \\
h^b v^b &= (-n_y^2 + n_t^2 + n_x^2)h^l v^l - (2n_t n_y)h^l - (2n_x n_y)h^l u^l.
\end{aligned}
\tag{68}
$$

5.1. Burgers' solution

The one-dimensional shallow water equations with $h_b = 0$ take the form of Burgers' equation $\partial_t q + q\partial_x q = 0$, when one of its Riemann invariants is taken constant as $u + 2\sqrt{gh} = c$ with $q(t,x) = c - 3\sqrt{gh}$. A solution can be constructed as $h(t,x) = (q(t,x) - c)^2/(9g)$ and $u(t,x) = (c + 2q(t,x))/3$ from the implicit solution $q(t,x) = q_0(x'), x = x' + q_0(x')t$, where $q(0,x) = q_0(x)$ is the initial condition. For an initial condition $q_0(x)$ with $dq_0/dx < 0$ somewhere, wave breaking occurs at time $t_b = -1/\min(dq_0/dx)$.

We chose $c = 3$, $q_0(x) = \sin(\pi x)$ with $x \in [0,2]$ and used periodic boundary conditions in x. The space–time profile of water depth for the exact and numerical solutions are shown in Fig. 9(a). The smooth initial condition develops into a discontinuity in a finite time $t < t_b = 1/\pi$ at $x = 1$. We can thus test Krivodonova's discontinuity detector, which shows no sign of discontinuity in the beginning and gradually detects the regions with sharp gradients to finally detect discontinuities as shown in Fig. 9(b). Before breaking, we compute several errors for mass, h and momentum, hu, on various meshes and plot them on a log–log scale in Fig. 10(a) and (b). They indicate that the method is second-order accurate in space and time.

5.2. Dispersion and dissipation error

To quantitatively verify the Fourier analysis, we consider the following harmonic wave type solution based on (47) in a domain $[0, L_x]$ with $h(t,x) = H + A\sin(kx + \omega t)$ and velocity corresponding to the real part of (48). In Section 4.2, we have presented the discrete Fourier analysis of equations (47) to determine the numerical frequency ω_1 and the numerical dissipation ω_2 of a given harmonic wave from (57). Here, we initialize with the harmonic wave solution based on (47) in the non-linear numerical code, for small amplitude, and compare our numerical simulations both with the exact solutions and discrete Fourier solutions. The discrete Fourier
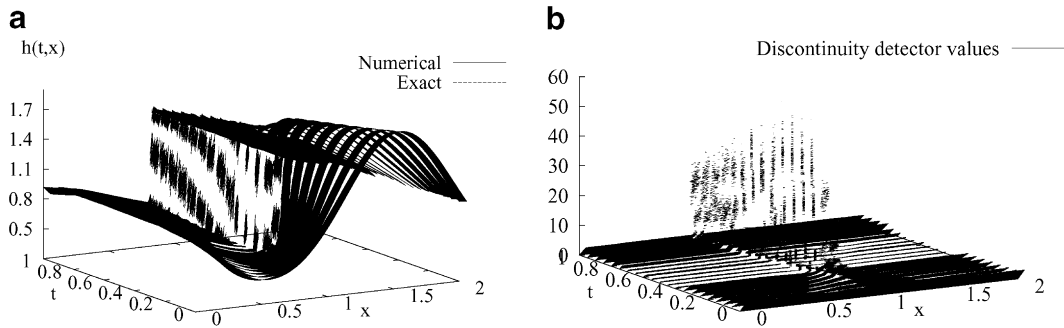
Fig. 9. (a) Comparison of exact and numerical solutions of water depth $h(t,x)$. (b) Plot of the discontinuity detector. Computations are performed on an irregular grid of 160×160 elements from $t = 0$ to the time of breaking $t_b \approx 0.3$ and $t_b < t < 1$. Irregular grids are made by a slight, random perturbation of the interior grid points of a rectangular mesh.
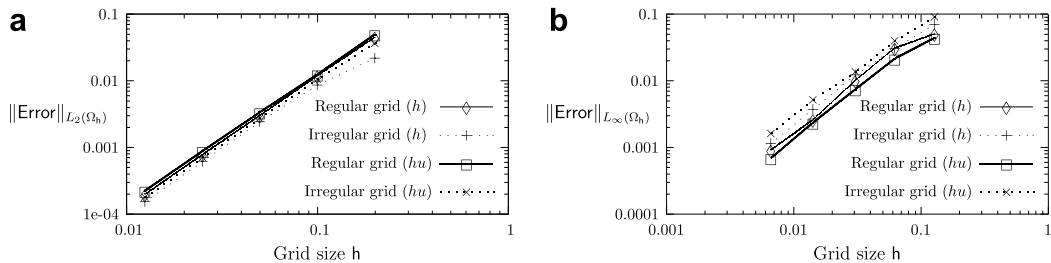

Fig. 10. (a) Log–log plot of the $\|Error\|_{L^2(\Omega_h)}$ versus grid size h at $t = 0.2$. The average slope of the curves is 1.955, 1.7875, 1.83 and 1.795 for h and hu on regular and irregular grids, respectively. (b) Log–log plot of the $\|Error\|_{L^\infty(\Omega_h)}$ versus grid size h at $t = 0.2$. The average slope of the curves is 1.32, 1.39, 1.16 and 1.39 for h and hu on regular and irregular grids, respectively. Regular grids are tessellated with 10, 20, 40, 80 and 160 elements and irregular grids with $10 \times 10, 20 \times 20, 40 \times 40, 80 \times 80$ and 160×160 elements. Computations are performed with time steps $\Delta t = 0.05, 0.025, 0.0125, 0.0625$ and 0.003125 from coarse to fine grids.

solutions can be simply given by replacing frequency ω by ω_1 and amplitude A by $A\exp(-\omega_2 t)$. Fig. 11(a) and (b) shows the exact and numerical solution at $t = 3.0$ for $f = 2\pi$, respectively. Observe the phase decay of amplitude of the waves in Fig. 11. We conclude that our numerical scheme confirms the Fourier analysis.

5.3. Poincaré and Kelvin waves

Poincaré and Kelvin wave solutions arise when we solve the linearized rotating shallow water equations in rectangular channel and circular basins. We simulate the non-linear counterparts of these harmonic waves at low amplitude for a number of time periods to show the dispersion and dissipation error.

5.3.1. Rectangular channel
Both Poincaré and Kelvin waves [15] are simulated for ten time periods in a rectangular channel periodic in x. Dispersion errors and dissipation errors are observed in the numerical solutions displayed in Figs. 12 and 13.
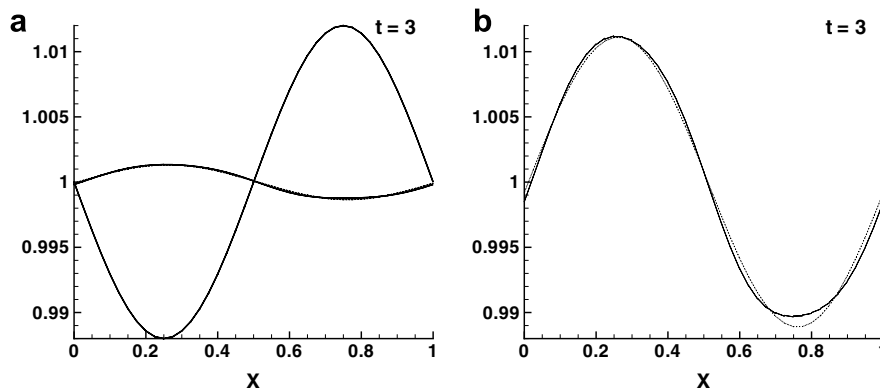
Fig. 11. Free surface plots showing (a) the dissipation in a comparison of the exact versus exact discrete and numerical solution and (b) the dispersion of the exact discrete and numerical solution for $f = 2\pi$, $k = 2\pi$, $g = 1$ and $H = 1$ with $\omega_1 = 8.3535$ and $\omega_2 = 0.73235$ for $\Delta x = 0.025$ and $\Delta t = 0.25$. We purposely chose a case with strong dissipation for illustrative purposes.
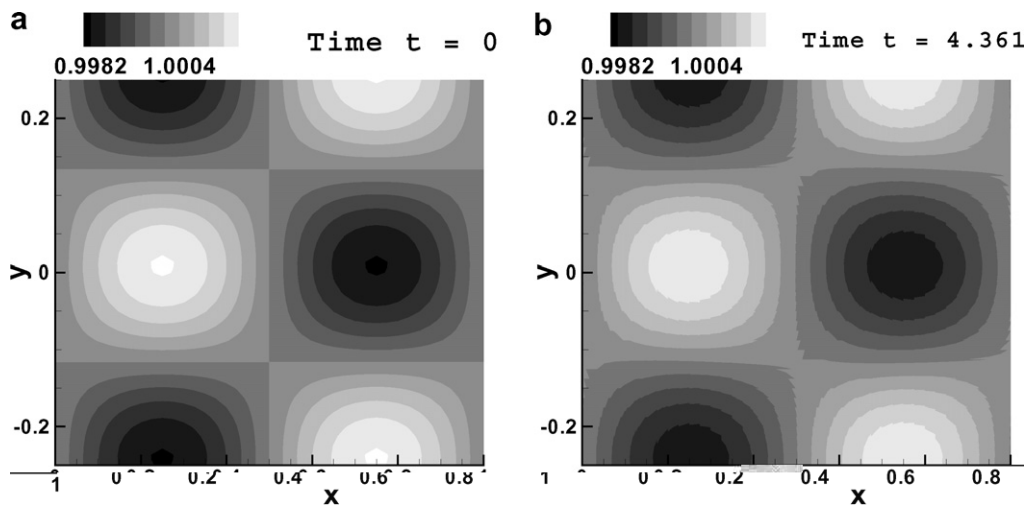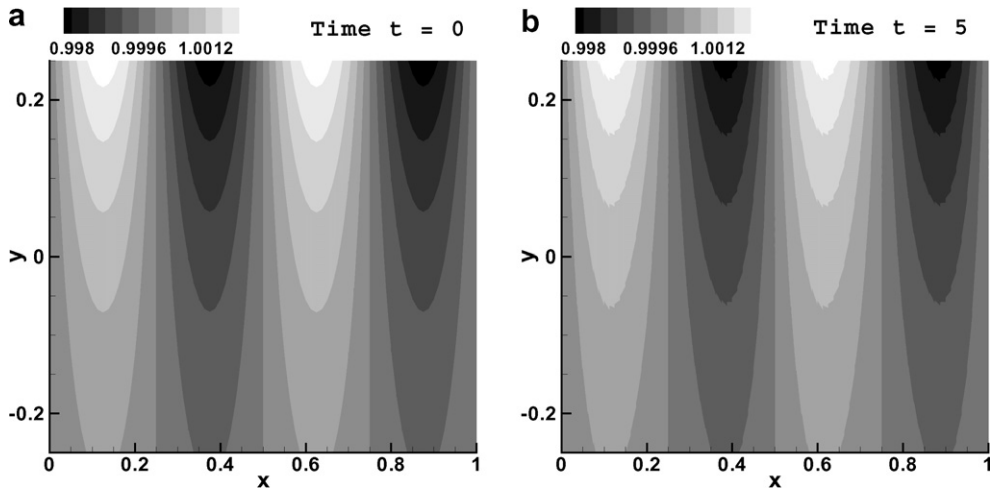

Fig. 12. Contour plots of the free surface for Poincaré waves (a) at $t = 0.0$ and (b) at $t = 10T$. The linear wave amplitude is $A(\omega l \cos(ly) + fk\sin(ly))\sin(kx + \omega t)$ with wave numbers k, l, and frequency $\omega = \sqrt{f^2 + a^2(k^2 + l^2)}$. The wave amplitude is 10^{-5}, zonal and meridional wave numbers are $m = n = 1$, $g = H = 1$, and $f = 3.193379349$. Simulated on a mesh of size 80×40 elements with $\text{CFL}_{\Delta t} = 1.0$. (a) Initial profile and (b) final profile.

5.3.2. Circular basin

We numerically simulate Poincaré and Kelvin waves [11], the former from $t = 0, \ldots, 10T$ with $T = 2\pi/\omega = 0.7217287851$ in a circular basin. Fig. 14 shows contour plots of the free surface for Poincaré waves and the difference between the exact linear and numerical non-linear solutions. The Kelvin wave mode has a time period $T = 2\pi/\omega = 7.356451577$ and we numerically simulate these waves from $t = 0, \ldots, 5T$ (see Fig. 15). In both cases the differences are small as expected for small-amplitude waves.

Fig. 13. Contour plots of the free surface for Kelvin waves (a) at $t = 0.0$ and (b) at $t = 10T$. Linear wave amplitude is $A(\cosh(ly) + \sinh(ly))\sin(kx + \omega t)$ with wave amplitude $A = 0.001$, $l = f/a$, $\omega = ak$, zonal wave number $m = 2$, $g = H = 1$ and $f = 3.193379349$. Simulated on a mesh of size 80×40 elements with $\text{CFL}_{\Delta t} = 1.0$. (a) Initial profile and (b) final profile.
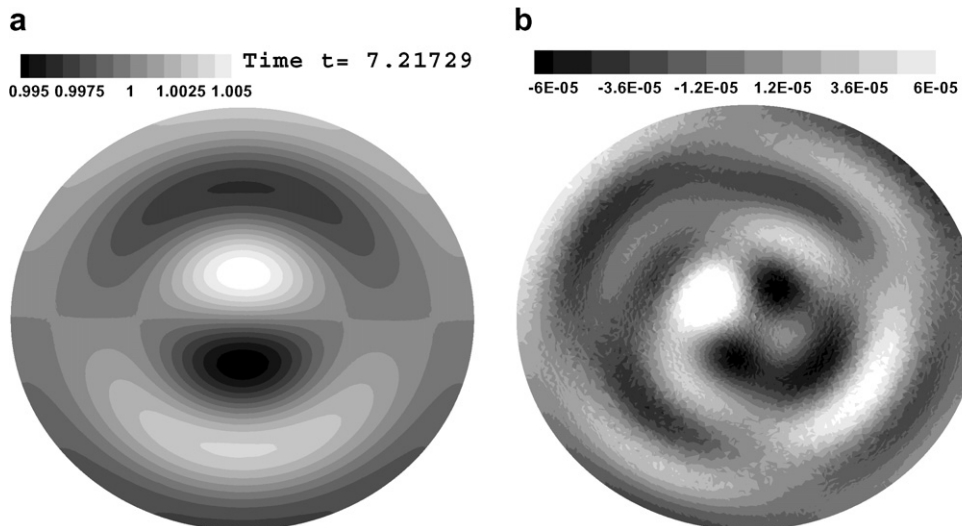
Fig. 14. Contour plots of (a) free surface of the Poincaré waves, and (b) the difference between linear exact and non-linear numerical solutions after ten time periods. Linear wave amplitude is $AJ_m(kr)\sin(m\theta + \omega t)$ with Bessel function $J_m(kr)$, radius r, azimuth θ, domain radius $R = 1$, azimuthal wave number $m = 1$, $f = 1.596689674$, $A = 0.01$, $H = 1$, $R = 1$, $g = 1$, radial wave number $k = 8.558068886$ obtained from the boundary condition, and $\omega = 8.705742988$. (a) Final profile and (b) difference.
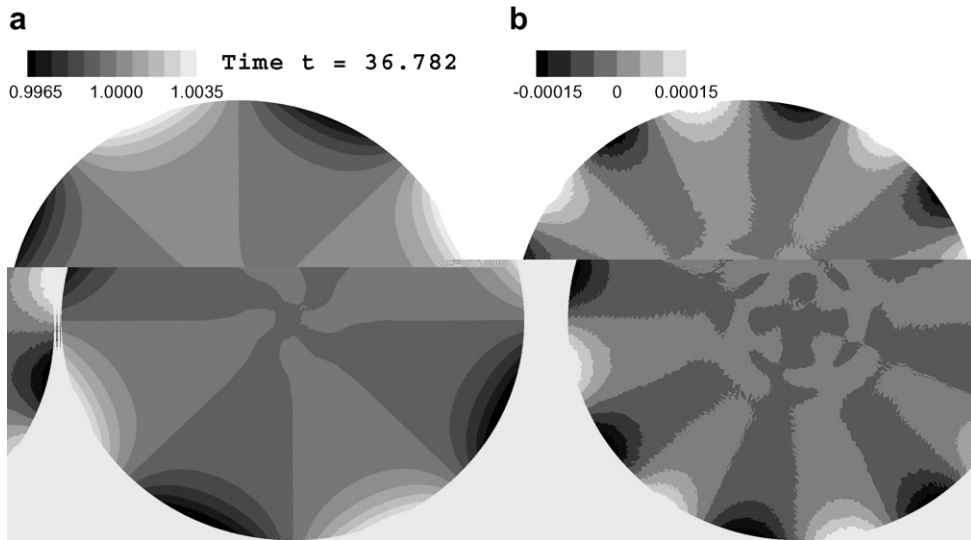
Fig. 15. Contour plots of (a) free surface of the Kelvin waves, and (b) difference between linear exact and non-linear numerical solutions at $t = 5T$. Linear wave amplitude is $AI_m(kr) \sin(m\theta + \omega t)$ with modified Bessel function $I_m(kr)$, $m = 4$, $f = 1.596689674$, $A = 10^{-5}$, $R = 5$, $g = H = 1$, $k = 1.349044778$ and $\omega = -0.8541054396$. (a) Final profile and (b) difference.

5.4. Moving grid simulations

5.4.1. Harmonic wave maker

Consider the linearized shallow water equations $\partial_t \eta + H\overline{\nabla} \cdot \mathbf{u} = 0$ and $\partial_t \mathbf{u} + g\overline{\nabla}\eta = 0$ in a rectangular basin of size $[(0, L_x) \times (0, L_y)]$ with a solid wave maker at the boundary $x_E(t, y) = L_x + x_m(t, y)$, fixed solid walls on the remaining boundaries, free surface perturbation $\eta(\mathbf{x})$ around a mean surface H, and velocity field $(u(\mathbf{x}), v(\mathbf{x}))$. After applying the kinematic boundary condition at the wave maker and linearizing the resulting expression, we obtain $\partial_t x_m = u(t, x = L_x, y)$. A linear gravity-wave type solution follows as

$$
\begin{aligned}
(\eta(\mathbf{x}), x_m(t, y)) &= \eta_0 \big(\cos(kx), -gk \sin(kL_x)/\omega^2\big) \cos(ly) \sin(\omega t), \\
(u(\mathbf{x}), v(\mathbf{x})) &= -gk\eta_0(k, l) \sin(kx) \cos(ly) \cos(\omega t)/\omega,
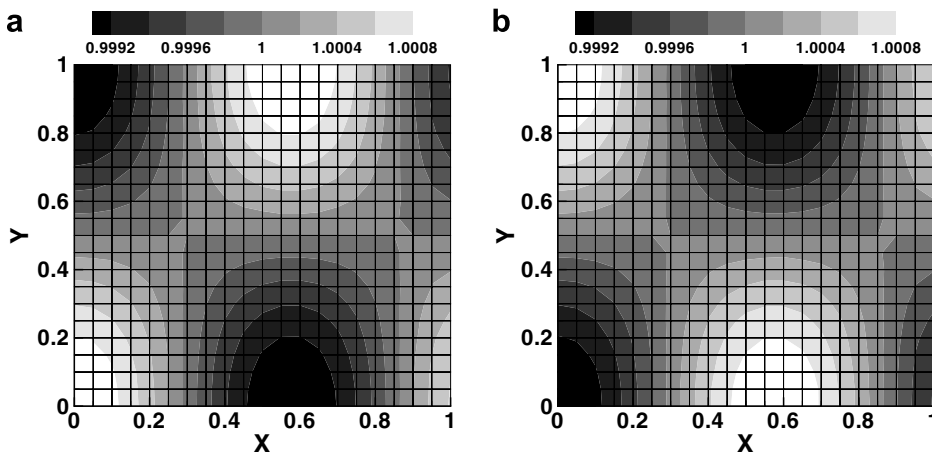\end{aligned}
\tag{69}
$$

Fig. 16. Contour plots of water depth h for a time period $T = 2\pi/\omega = 1.0$. Parameters $g = 1$, $H = 1$, $\eta_0 = 0.001$, $n = 1$ and $m = \sqrt{3}$ such that $\omega = 2\pi$. At $t = T/2$ and T, the free surface is nearly flat. (a) At $t = T/4$ and (b) at $t = 3T/4$.
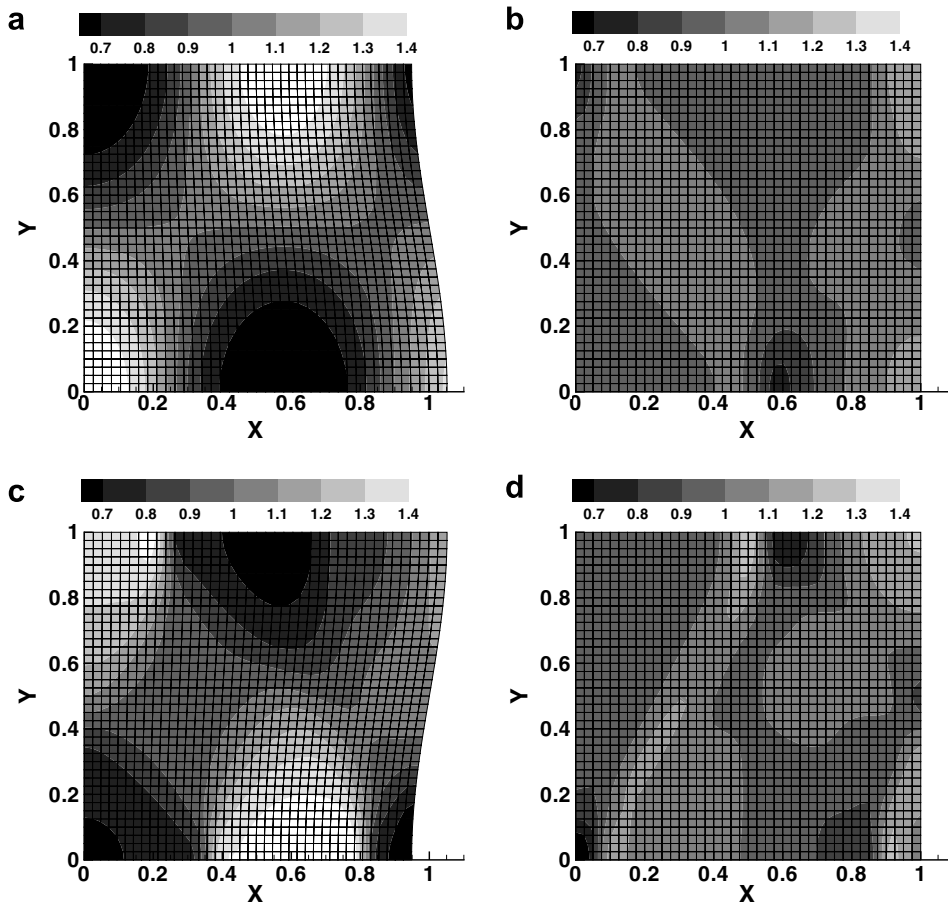
Fig. 17. Contour plots of water depth h for a time period $T = 2\pi/\omega = 1.0$. Parameters $g = 1$, $H = 1$, $\eta_0 = 0.5$, $n = 1$ and $m = \sqrt{3}$ such that $\omega = 2\pi$. (a) At $t = T/4$, (b) at $t = T/2$, (c) at $t = 3T/4$ and (d) at $t = T$.

where η_0 is the amplitude of the harmonic free surface waves, ω the frequency determined from the dispersion relation $\omega^2 = gH(k^2 + l^2)$ once $l = n\pi/L_y$ the wave numbers along y and $k = m\pi/L_x$ along x are known, with n an integer and m a real number.

We initialize the non-linear equations using the gravity wave solution (69) at $t = 0$, and prescribe the movement of the wave maker at $x = L_x$ to simulate the waves induced. To maintain elements of regular size, we move the nodes of the grid by linearly interpolating between the wave maker and the solid wall at $x = 0$. Thus, given the coordinates of a node at time t_{n-1}, it is straightforward to determine these at time t_n. We simulate the non-linear waves generated by the harmonic wave maker for low and high amplitudes. At low amplitude, we see that harmonic waves in the wave maker agrees qualitatively with the solution (69), see Fig. 16 and at high amplitudes, these harmonic waves start to break due to non-linearity and moving bores are formed, see Fig. 17. For low amplitude the energy stays essentially constant, while for high amplitude the energy fluctuates but initially decreases on average due to wave breaking, see Fig. 18.

6. Validation

In this section, we validate numerical simulations of bore–vortex or bore–shear interactions against the qualitative analytical predictions of PV anomaly from the expression (10). In each of the three cases presented, there is initially no PV, but PV is generated through the passage of a non-uniform bore. We verified the simulations against Tassi et al.'s [21] who used a space DG method.
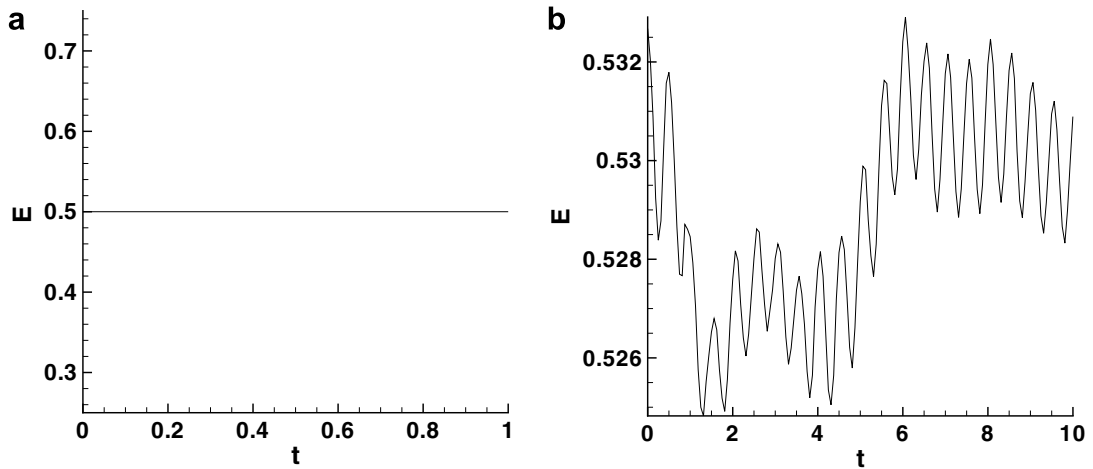
Fig. 18. Plots of the energy as a function of time in the wave maker test. (a) Low amplitude and (b) high amplitude.

6.1. Non-linear breaking shallow water waves

We consider the linear gravity wave solution

$$\eta(\mathbf{x}) = A \sin(ly) \sin(kx + \omega t),$$
$$(u(\mathbf{x}), v(\mathbf{x}))^{\mathrm{T}} = Ag(-k \sin(ly) \sin(kx + \omega t), l \cos(ly) \cos(kx + \omega t))^{\mathrm{T}}/\omega \tag{70}$$

in a rectangular domain of size $[L_x, L_y]$ periodic in x with solid walls along y, $k = 2\pi m/L_x$, $l = (2n + 1)\pi/L_y$, and $\omega^2 = gH(k^2 + l^2)$. The non-linear numerical discretization is initialized with this linear solution (70) at $t = 0.0$ with $A = 0.01$, $g = H = 1$, $m = 2$ and $n = 0$.

Due to non-linearity, these higher amplitude gravity waves start to break around $t \approx 0.5$, which can be confirmed from the energy–time graph shown in Fig. 20(a). The breaking of the waves is first seen at the peak of crests and troughs of the free surface near to the walls, see Fig. 19(a) and (b). As seen in Fig. 21(a), the breaking extends to the interior and moving bores are formed which are aligned in the y-direction with some curvature. Since the non-uniform depth profile of the bore appears to be preserved in time, we estimate its upstream and downstream depths from (70) as

$$h_1(\hat{y}) = H - \eta_{\mathrm{D}}(\hat{y}) \quad \text{and} \quad h_2(\hat{y}) = H + \eta_{\mathrm{D}}(\hat{y}), \tag{71}$$
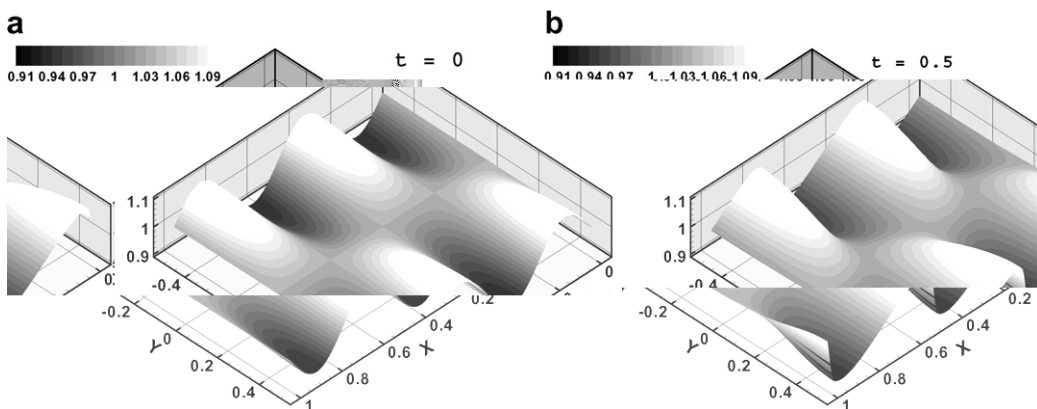

Fig. 19. Free surface height of the water at (a) $t = 0.0$ and (b) $t = 0.5$.

respectively, with $\eta_D(\hat{y}) = |\hat{A}|\sin(\pi\hat{y})$, $\hat{A}$ the amplitude and $\hat{y}$ the axis aligned along the bore neglecting the curvature of the bore. These bores are traveling in the negative x-direction with their axis $\hat{y}$ roughly parallel to the direction of y-axis. Substituting the depths (71) in (10), we get the PV generation behind the bore as

$$\Delta\Pi = \Pi_1 - \Pi_2 = \frac{2g\eta_D^2(3H^2 - \eta_D^2)}{(H^2 - \eta_D^2)^2}\left(\frac{-1}{Q}\frac{d\eta_D}{d\hat{y}}\right). \tag{72}$$

For $-0.5 < y < 0$, we have $d\eta_D/d\hat{y} > 0$, $h_1 > h_2$, $Q < 0$ and $\Delta\Pi > 0$; and for $0 > y > 0.5$, we have $d\eta_D/d\hat{y} > 0$, $h_1 < h_2$, $Q > 0$ and $\Delta\Pi < 0$. Hence, the PV generated in Fig. 21(b) has a positive sign on the positive y axis and vice versa. Also see the zonal average of PV along the grid lines parallel to x-axis in Fig. 20(b). This qualitatively validates the bore–vortex anomaly discussed in Section 2.

The bores formed are simulated till $t = 25$ when they have dissipated their energy as seen in Fig. 20(a). As a result, we see a PV jet formation near to the walls, shown in Fig. 21(d)–(f). Due to energy dissipation, the strength of the bores gradually decreases as in Figs. 21 and 22(a), and finally the bores disappear in Fig. 22(c)–(e). Although the bores disappear, the jet remains since PV is materially conserved (see Fig. 22(d)–(f)).
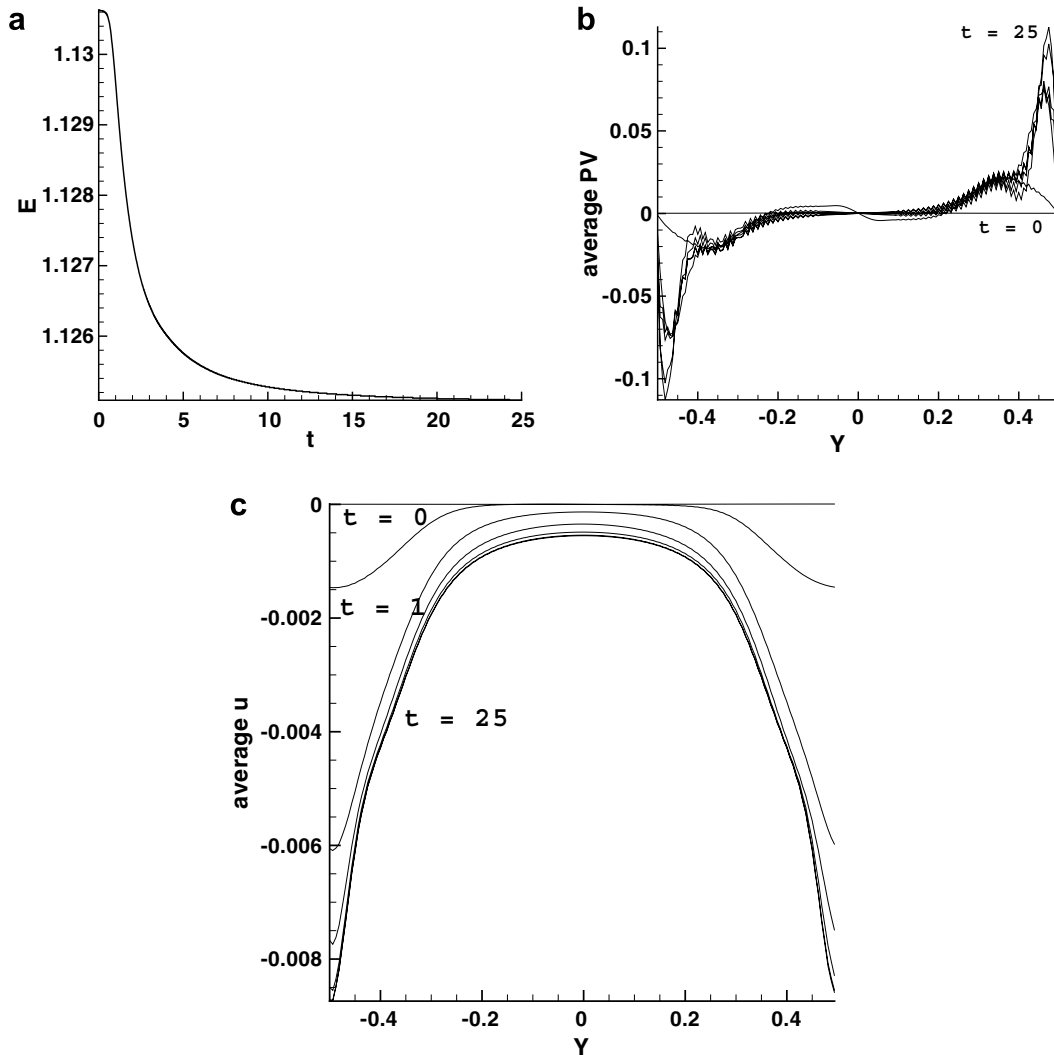

Fig. 20. Shown are (a) the energy $E = E(t) = \int_\Omega \bar{E}(\mathbf{x}, t)\,dx\,dy$ (cf. 4) as function of time, (b) profiles of PV averaged along the channel as a function of y, (c) profiles of u averaged as a function of y at various times.
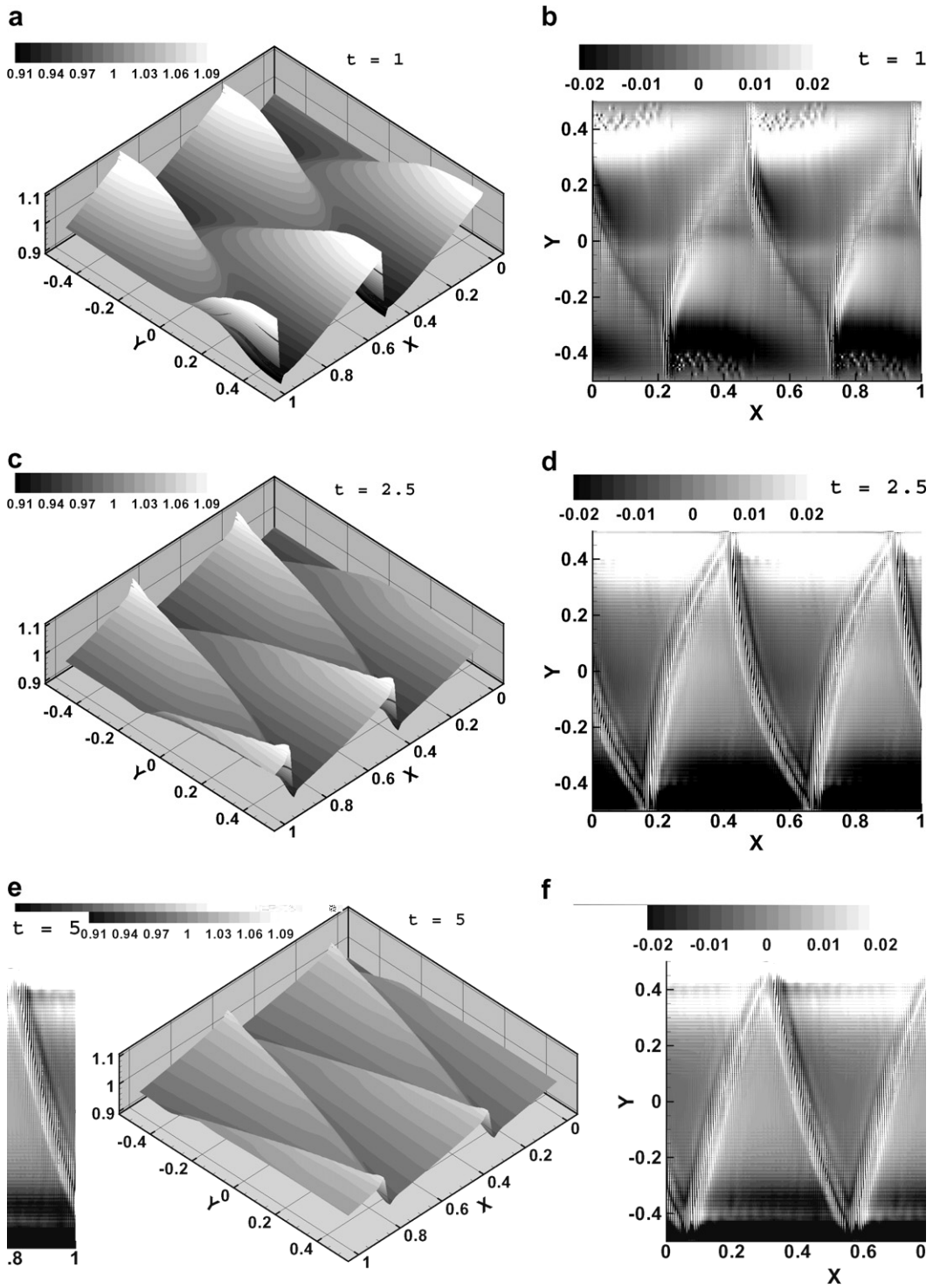
Fig. 21. (a) Free surface height of the water and (b) shadow graph of the PV generated at $t = 1.0$. Observe the PV generation has opposite signs. (c) and (d) Same at $t = 2.5$. (e) and (f) Same at $t = 5.0$.
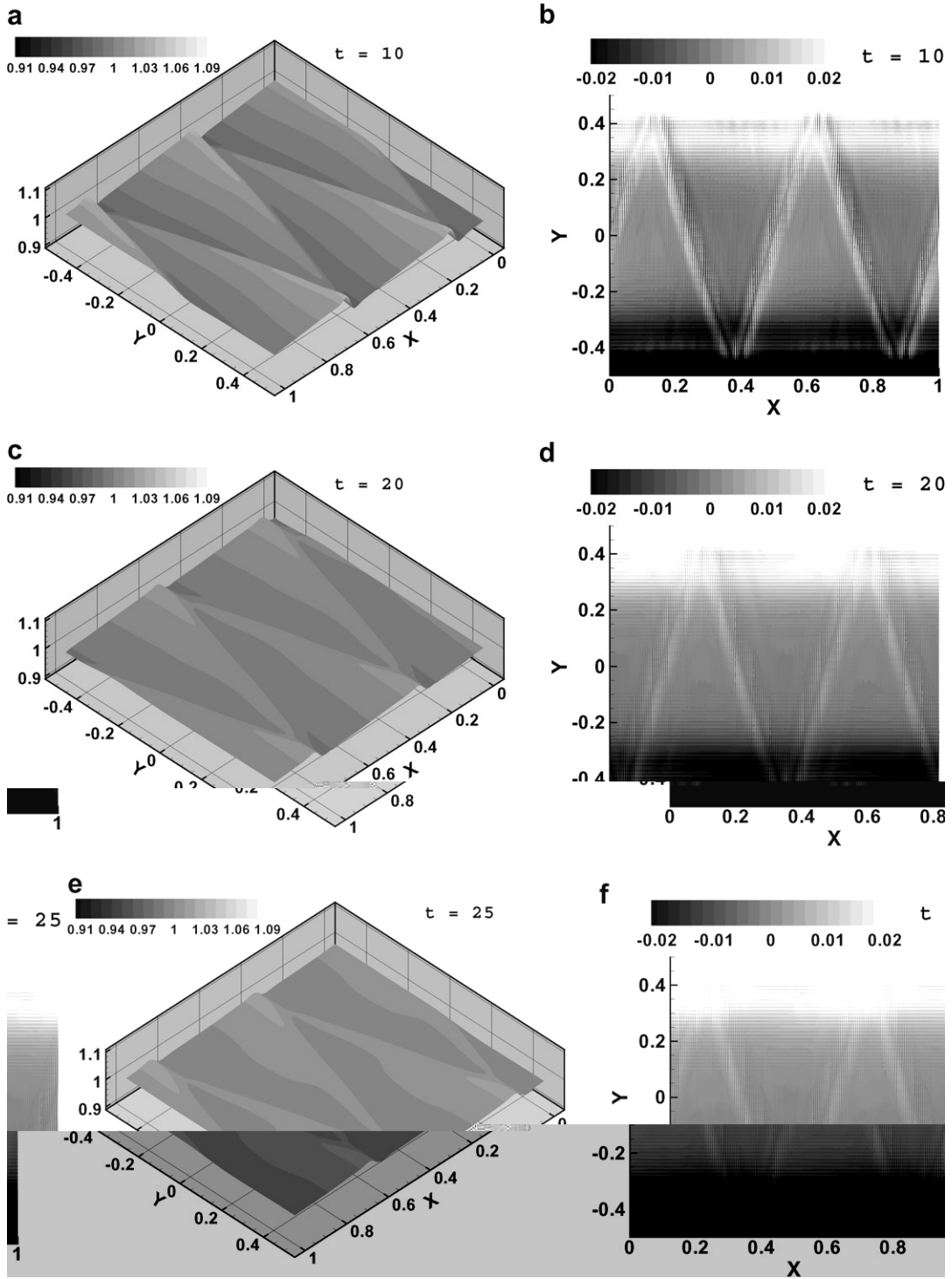
Fig. 22. (a) Free surface height of the water and (b) shadow graph of the PV generated at $t = 10$. (c) and (d) Same at $t = 20$. (e) and (f) Same at $t = 25$.

6.2. Bore propagation over a mound

6.2.1. Conical shaped mound

Matsutomi and Mochizula [13] conducted experiments to study the behavior of a bore propagating over a conical shoal and Hu [7] conducted numerical simulations of these experiments.

We show similarly that the correct PV anomaly is generated in our numerical simulation due to non-uniform energy dissipation along the bore.

Consider the dam-break initial condition $h(0, \bar{\mathbf{x}}) + h_b(\bar{\mathbf{x}}) = h_L$ for $x < x_c$, $h(0, \bar{\mathbf{x}}) + h_b(\bar{\mathbf{x}}) = h_R$ for $x > x_c$ and water at rest $\mathbf{u}(0, \bar{\mathbf{x}}) = 0$, where $x = x_c$ is the discontinuity in a rectangular channel of size $[0, L_x] \times [0, L_y]$. Let an isolated conical shaped mound be situated with its center at $\bar{\mathbf{x}}_m = (x_m, L_y/2)$, radius R_m, height H_m. The bottom topography in the channel is

$$h_b(\mathbf{x}) = \begin{cases} H_m - \frac{H_m}{R_m} |\bar{\mathbf{x}} - \bar{\mathbf{x}}_m|, & \text{if } |\bar{\mathbf{x}} - \bar{\mathbf{x}}_m| \leqslant R_m, \\ 0.0, & \text{if } |\bar{\mathbf{x}} - \bar{\mathbf{x}}_m| > R_m. \end{cases} \tag{73}$$

The boundaries of the domain consist of solid walls except for an open boundary at $x = L_x$.

When the dam collapses, a bore with uniform jump is generated which propagates towards and over the conical hump, see Fig. 23, and dissipates energy uniformly along its length. When the bore reaches the conical hump energy dissipation becomes non-uniform and the approximate PV generation (10) across the bore is

$$\Pi_1 - \Pi_2 \approx \frac{E_D}{Q} \left(\frac{1}{h_1} + \frac{1}{h_2} \right) (-\partial_y h_b), \tag{74}$$

with $h_1 \approx h_L - h_b$ and $h_2 \approx h_R - h_b$, since we always observe a nearly uniform jump in the free surface along the bore in our numerical simulations and $\hat{y}$ is aligned with y. For $y > L_y/2$, we have $-\partial_y h_b > 0$ and vice versa for $y < L_y/2$. Hence, a positive PV anomaly arises for $y > L_y/2$ and a negative one for $y < L_y/2$ after the bore has passed. This is confirmed in the contour plots of PV shown in Fig. 24: a positive vortex and PV are found for $y > L/2$ and vice versa for $y < L/2$ after the bore's passage. Thereafter, these PV anomalies are advected along, cf. (5).

6.2.2. Gaussian shaped mound

In this test case, we also consider an initial dam break as $h(0, \bar{\mathbf{x}}) + h_b(\bar{\mathbf{x}}) = h_L$ for $x < x_c$, $h(0, \bar{\mathbf{x}}) + h_b(\bar{\mathbf{x}}) = h_R$ for $x > x_c$ and water at rest $\mathbf{u}(0, \bar{\mathbf{x}}) = 0$. The discontinuity in the free surface lies thus at $x = x_c$ in a rectangular channel of size $[0, L_x] \times [0, L_y]$. It has solid wall boundaries except for an open flow boundary at $x = L_x$. The bottom topography consists of an isolated Gaussian shaped mound with a peak at $\bar{\mathbf{x}}_m = (L_x/2, L_y/2)$
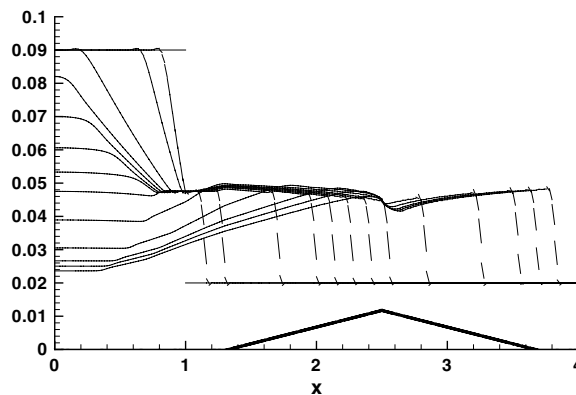

Fig. 23. A bore propagates over a conical mound: profiles of the free surface $h + h_b$ are shown at $y = 1.3$ from time $t = 0$ to 10 with steps of 0.5. Topography h_b is also displayed.
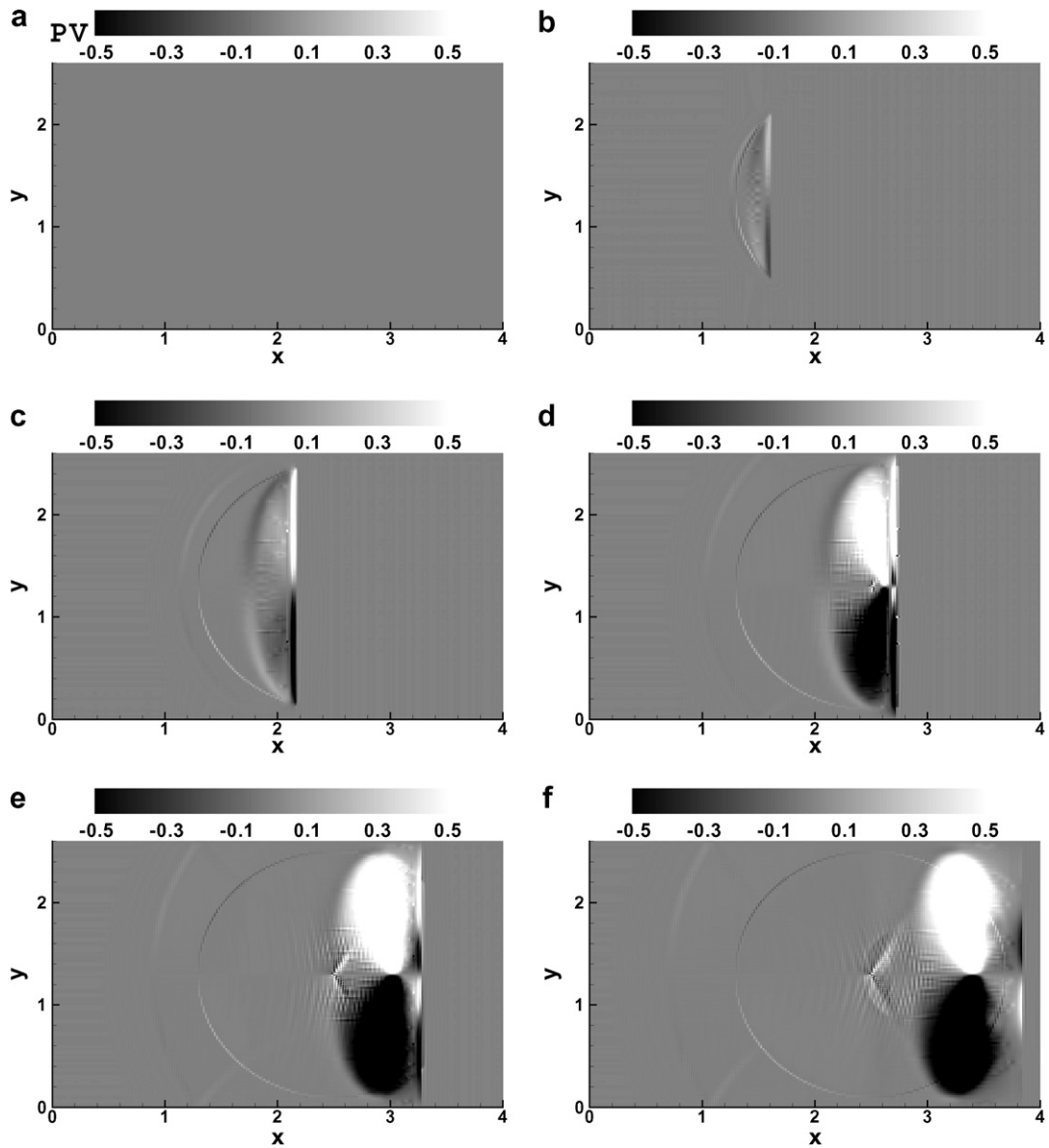
Fig. 24. Conical mound case. (a)–(f) Shows the contour plots of the PV at times $t = 0,\ 2,\ 4,\ 6,\ 8$ and 10. Note that PV is zero at $t = 0$. Computations are performed on a grid of size 200×130. Parameters are $L_x = 4.0,\ L_y = 2.6,\ x_m = 2.5,\ R_m = 1.2$ and $H_m = 0.012$.

$$h_b(\mathbf{x}) = H_m \exp(-c_m|\bar{\mathbf{x}} - \bar{\mathbf{x}}_m|^2), \tag{75}$$

where H_m is the height of the Gaussian mound and c_m a constant.

When the initial dam collapses, a bore with a uniform jump is generated which propagates towards the Gaussian mound, see Fig. 25. As the bore reaches the Gaussian mound, we deduce from (74) that the potential vorticity generated behind the bore must have positive sign for $y > L_y/2$ as $\partial_y h_b < 0$ and negative sign for $y < L_y/2$ as $\partial_y h_b > 0$. Hence, the PV generated and seen in Fig. 25(b) and (c) agrees with the observed one. Once the bore crosses the peak of the hump, a hydraulic jump facing backwards is formed which can be seen as a depression in Fig. 25. Thus, it can likewise be deduced that PV anomalies are generated at the hydraulic jump with opposite signs to the initial PV generated at the bore, which is confirmed in Fig. 26(d).
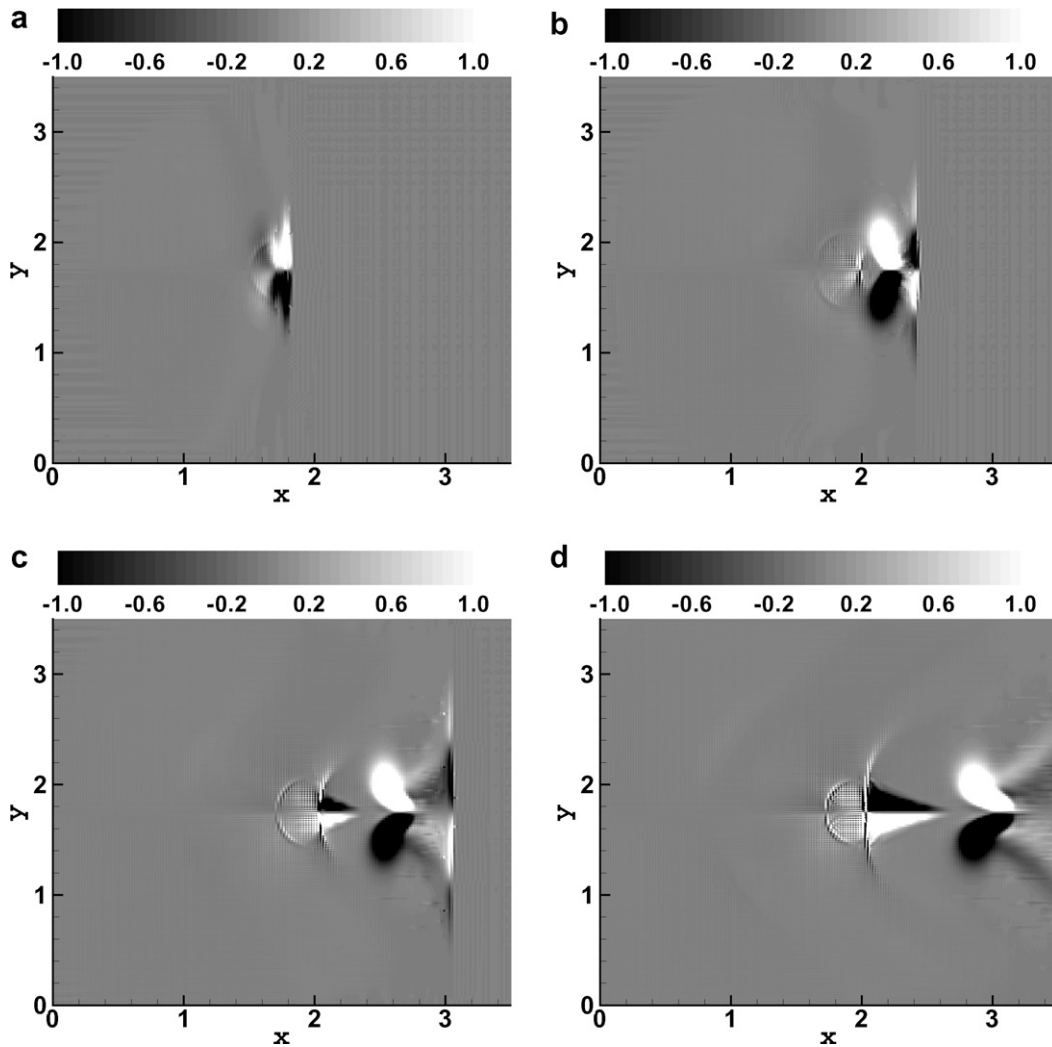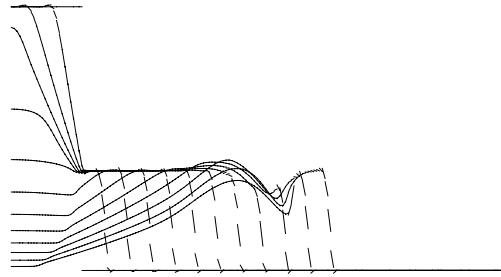
Fig. 26. Gaussian mound case. Displayed are contour plots of PV at various times. Note that initially PV is zero. Computations are performed on a grid of size 175×175. We chose $L_x = L_y = 3.5$, $x_c = 0.5$, $h_L = 0.11$, $h_R = 0.02$, $H_m = 0.01$ and $c_m = 12.5$. (a) $t = 4$, (b) $t = 6$, (c) $t = 8$ and (d) $t = 10$.

7. Conclusions

A space–time discontinuous Galerkin method for the (rotating) shallow water equations has been presented for shallow flows over varying topography and in time dependent domains. This application of the space–time discontinuous Galerkin method is new. It is especially interesting as a mile stone towards accurate numerical modeling of the time evolution of the water line in flooding and drying events. These events are important in the prediction of river floods and near-shore hydrodynamics.

Due to the presence of bores in the shallow water equations spurious oscillations will arise in higher order shock-capturing numerical schemes such as our space–time method. We have limited these spurious oscillations around discontinuities and sharp gradients by applying dissipation but only near discontinuities once these are detected by Krivodonova's discontinuity detector [9]. Furthermore, we showed that our numerical discretization preserves the state of rest for non-uniform topography, by use of a smooth approximation for the topography. A discrete Fourier analysis of the numerical discretization for one-dimensional linearized rotating shallow water equations showed that the scheme was unconditionally stable with small dispersion and dissipation error.

We have thoroughly verified the present method by testing the order of accuracy and the application of the discontinuity detector in combination with the dissipation operator. The method was second-order accurate in space and time in the L^2 norm for a linear polynomial approximation of flow fields. We simulated small-amplitude gravity, Kelvin and Poincaré wave solutions for a number of time periods to observe the dispersion and dissipation errors. Of special importance was the validation of the numerical discretization by simulating bore–vortex interactions, which could be compared with analytical results on the generation of PV anomaly by non-uniform bores. The relevance of these bore–vortex interactions in testing numerical schemes has been promoted in work by Hu [7] and Peregrine [16]. Several demanding cases were considered in Section 6: PV and shear formation by breaking waves in a periodic channel, and the generation of PV and vortices by an initially uniform bore over non-uniform topography. Finally, the versatility of the present method in dynamic domains has been demonstrated numerically in Section 5.4.1. We considered the generation of nearly linear and highly non-linear waves by prescribing the motion of a flexible domain wall as a wave maker. It showed that the space–time DG method seems well suited for improved simulation of run-up and backwash on beaches [5] and in flood prediction.

References

[1] V.R. Ambati, Flooding and drying in discontinuous Galerkin discretizations of shallow water equations. ECCOMAS Egmond aan Zee 2006, European Conference on CFD. http://proceedings.fyper.com/eccomascfd2006/, 2006.

[2] V.R. Ambati, O. Bokhove, Space–time discontinuous Galerkin finite element method for shallow water flows, J. Comput. Appl. Math. (2006), doi:10.1016/j.cam.2006.01.047.

[3] E. Audusse, M.-O. Bristeau, A well-balanced positivity preserving "second-order" scheme for shallow water flows on unstructured grids, J. Comput. Phys. 206 (2006) 311–333.

[4] P. Batten, N. Clarke, C. Lambert, D.M. Causon, On the choice of wavespeeds for the HLLC Riemann solver, SIAM J. Sci. Comput. 18 (6) (1997) 1553–1570.

[5] O. Bokhove, Flooding and drying in finite-element Galerkin discretizations of shallow water equations. Part I: one dimension, J. Sci. Comput. 22 (2005) 47–82.

[6] O. Bühler, On the vorticity transport due to dissipating or breaking waves in shallow-water flow, J. Fluid Mech. 407 (2000) 235–263.

[7] G. Hu, Note on numerical simulation of shallow water, Bristol University, School of Mathematics, Rep. No. AM-02-01, 2002.

[8] J. Jaffre, C. Johnson, A. Szepessy, Convergence of the discontinuous Galerkin method for hyperbolic conservation laws, Math. Models Methods Appl. Sci. 5 (1995) 367–386.

[9] L. Krivodonova, J. Xin, J.-F. Remacle, N. Chevaugeon, J.E. Flaherty, Shock detection and limiting with discontinuous Galerkin methods for hyperbolic conservation laws, Appl. Numer. Math. 48 (2004) 323–338.

[10] A. Kurganov, D. Levy, Central-upwind schemes for the Saint-Venant equations, Math. Model. Numer. Anal. 36 (2002) 397–425.

[11] H. Lamb, Hydrodynamics, Dover Publications, New York, 1932.

[12] R.J. LeVeque, Numerical Methods for Conservation Laws, Birkhäuser Verlag, Berlin, 1992.

[13] H. Matsutomi, A. Mochizula, Behaviour of a bore over a conical shoal, Tohoku J. Natural Disaster Sci. 37 (2001) 67–73 (in Japanese).

[14] S. McCormick, B. Briggs, V. Henson, A Multigrid Tutorial, SIAM, Philadelphia, 2000.

[15] J. Pedlosky, Geophysical Fluid Dynamics, Springer, New York, 1998.

[16] D.H. Peregrine, Surf zone currents, Theor. Comput. Fluid Dyn. 10 (1998) 295–309.

[17] L.J. Pratt, On inertial flow over topography, Part 1: Semigeostrophic adjustment to an obstacle, J. Fluid Mech. 131 (1983) 195–218.

[18] S. Rhebergen, O. Bokhove, J.J.W. van der Vegt, Discontinuous Galerkin finite element methods for hyperbolic nonconservative partial differential equations. J. Comput. Phys., submitted for publication, http://eprints.eemcs.utwente.nl/ 2007.

[19] A.H. Shapiro, The Dynamics and Thermodynamics of Compressible Fluid Flow, Ronald, New York, 1953.

[20] J.J. Stoker, Water Waves: The Mathematical Theory with Applications, Interscience publishers, New York, 1957.

[21] P. Tassi, O. Bokhove, C. Vionnet, Space discontinuous Galerkin method for shallow water flows – kinetic and HLLC flux, and potential vorticity generation, Adv. Water Resour. 30 (4) (2007) 998–1015.

[22] E.F. Toro, Shock-capturing Methods for Free-surface Flows, Wiley, Toronto, 2001.

[23] E.F. Toro, M. Spruce, W. Speares, Restoration of the contact surface in the HLL-Riemann solver, Shock Waves 4 (1994) 25–34.

[24] J.J.W. van der Vegt, H. van der Ven, Space–time discontinuous Galerkin finite element method with dynamic grid motion for inviscid compressible flows, J. Comput. Phys. 182 (2002) 546–585.

[25] A.W. Vreman, M. Al-Tarazi, J.A.M. Kuipers, M. van Sint Annaland, O. Bokhove, Supercritical shallow granular flow through a contraction: experiment, theory and simulation, J. Fluid Mech. 578 (2007) 233–269.